DOE/ET-53088-232 IFSR #232

Particle Simulations of Current Driven Drift Waves in Shearless and Sheared Magnetic Fields

J. N. Leboeuf, D. R. Thayer, R. D. Sydora
and *P. H. Diamond*

Institute for Fusion Studies
The University of Texas at Austin
Austin, Texas 78712-1060

April 1986

Particle Simulations of Current Driven Drift Waves in Shearless and Sheared Magnetic Fields

J. N. Leboeuf, D. R. Thayer, R. D. Sydora, and *P. H. Diamond*

Institute for Fusion Studies

The University of Texas at Austin

Austin, Texas 78712-1060

Abstract

The nonlinear behavior of the collisionless current driven drift instability in shearless and sheared magnetic fields is studied by means of particle simulation. Electrostatic models with guiding center electrons and full dynamic ions are used in both two-and-one-half and three dimensions. The electron current ($J_{||}$), in the direction parallel to the magnetic field but perpendicular to the density gradient in the x direction, is maintained throughout the simulation. Instability thresholds, growth rates, real frequency spectra, and mode structures observed in the simulation are in good agreement with theory. Saturation of the unstable modes occurs by a flattening of the electron distribution function in (x, $v_{||}$) space. The measured potential saturation levels and final distribution functions are consistent with a quasilinear plateau theory for both shearless and sheared magnetic field configurations.

I. Introduction

It has long been recognized[1-3] that drift wave instabilities can give rise to anomalous transport in magnetically confined plasmas. Devices like tokamaks and reversed field pinches (RFP's) rely on a current flowing through the plasma to generate the poloidal field necessary for confinement. The possibility exists that current driven drift waves will be linearly destabilized even though the universal mode driven by the density gradient alone may be linearly stable under similar conditions. This in turn would enhance the transport and lead to a deterioration of confinement. For tokamaks, the ohmic current, as measured by the ratio of drift velocity to thermal velocity $(v_d/v_{\rm th})$, is too weak for the current driven drift waves to be unstable.[4-6] The situation is less clear for RFP's where $v_d/v_{\rm th}$ is frequently larger. In fact, it has recently been proposed that current driven drift waves may have a strong influence on both the confinement of the plasma and the (dynamo) sustainment of the magnetic field in RFP's.[7] Essentially, if the current driven drift waves are unstable, they generate potential and magnetic fluctuations which induce anomalous transport. The anomalous transport may also provide the drive for current diffusion needed for the dynamo action which maintains the field reversal. These observations are the principal motivation of our study.

The theory of current driven drift wave instabilities have been intensively studied previously.[4-6] Stability of current driven drift waves can be elucidated by reviewing well-known theory of the universal mode. A basic feature of the universal mode is that the presence of shear guarantees complete stabilization. For the universal mode in slab geometry, the nonresonant electrons close to the rational surface, when properly included in a linear theory, induce stability for all shear strengths.[8] For the current driven case, the resonance region is Doppler-shifted away from the rational surface at x_0 so that the stabilizing influence of the nonresonant electrons about x_0 is lost and only ion shear damping must be overcome for instability to occur. Previous particle simulations of current driven drift waves have been limited to cases without shear;[9] and no attempt has been made to maintain the current. The present study of current driven drift waves incorporates linear theory, nonlinear particle simulations, and a quasilinear theory of saturation. We consider slab geometry and treat the current driven drift waves in the electrostatic approximation

using guiding center electrons, full dynamic ions, and finite size particle codes in both two-and-one-half ($2\frac{1}{2}$D) and three (3D) dimensions.[10] Both shearless and sheared magnetic field configurations (one rational surface in $2\frac{1}{2}$D, multiple rational surfaces or helicities in 3D) have been implemented. We have chosen to maintain the parallel electron current or average drift throughout the simulation. No attempt was made to maintain the electron distribution function or the density gradient, and finite beta effects as well as toroidicity are absent from our electrostatic model.

Our principal results are summarized as follows. The simulations reproduce the instability thresholds, growth rates, real frequency spectra, and mode structures predicted by linear theory. The growth rate increases approximately linearly with drift velocity (v_d). Saturation of the instability is attributed to quasilinear plateauing of the electron distribution function in (x, $v_{||}$) space. The measured saturation levels and final altered distribution contours are in good agreement with a quasilinear theory. This theory reproduces the trend in the saturation level to increase roughly as $v_d^{1/2}$ in the shearless cases and as v_d in the sheared cases.

The remainder of this paper is organized in the following manner. Section II is devoted to a description of the computer code. A brief review of linear theory is given in Sec. III. Cases with shearless magnetic field are described in Sec. IV, while Sec. V is devoted to those with shear. The saturation mechanism is analyzed using a quasilinear plateau theory and compared with simulation in Sec. VI. Finally, a summary and discussion of the results is presented in Sec. VII.

II. Simulation Model

The computer code, the plasma parameter definitions, the plasma slab configuration, and its simulation realization are described in this section.

The simulation model is a 3D [spatial dimensions (x, y, z) and velocity dimensions (v_x, v_y, v_z)] electrostatic particle algorithm.[10] For particle motion, the guiding center approximation for electrons is used and full ion dynamics are followed. Perpendicular electron motion is therefore given by the $\vec{E} \times \vec{B}$ motion while parallel dynamics are followed exactly. The system is bounded by conducting walls at $x = 0$ and $x = L_x$ where the potential (ϕ) is set equal to zero. Particles are reflected at the walls so as to minimize sheath effects. The system is periodic in the y and z directions with lengths L_y and L_z, respectively. Particles are reintroduced in a periodic fashion for these two directions. The wave numbers in the y and z directions are expressed as $k_y = 2\pi m/L_y$; $m = 0, \pm 1, \ldots, \pm L_y/2$ and $k_z = 2\pi n/L_z$; $n = 0, \pm 1, \ldots, \pm L_z/2$. A two-dimensional grid is used in the (x, y) plane while a mode expansion is employed in the z direction where the charge density and force are evaluated at the exact particle positions. Typically no more than 10 modes of like sign out of a maximum of $L_z/2$ are kept in the expansion. For $k_z = 0$ or $n = 0$, the model reduces to the standard $2\frac{1}{2}$D one with spatial dimensions (x, y) and velocity dimensions (v_x, v_y, v_z).

The initial configuration is illustrated in Fig. 1. A strong confining magnetic field is externally imposed with $\vec{B} = B_0 (\hat{z} + \sin\theta \hat{y})$. For shearless cases, $\sin\theta$ is a constant; while for sheared cases, $\sin\theta = (x - x_0)/L_s$, where x_0 defines the location of the rational surfaces with respect to $x = 0$, and L_s is the shear length. Therefore, the wave number along the magnetic field is expressed as $k_{||} = \left(\vec{k} \cdot \vec{B}\right) / |\vec{B}| \approx k_z + k_y \sin\theta$. The positions of the rational surfaces in the sheared case are determined by $k_{||} = 0$ which yields $x_{mn} - x_0 = -\left(L_y L_s / L_z\right)(n/m)$. For the $2\frac{1}{2}$D sheared slab case there is only one rational surface at $x = x_0$.

Initially, the plasma has an exponential density profile, $n(x) = n_0 \kappa L_x \left\{\exp(-\kappa x)/\left[1 - \exp(-\kappa L_x)\right]\right\}$, and no temperature gradient. This profile gives a constant density gradient scale length L_n [$= 1/\kappa$, with $\kappa = -n'(x)/n(x)$]. The boundary conditions imposed on the potential are such that $\phi(0) = \phi(L_x) = 0$. The rational surfaces are located about $x_0 = L_x/2$, so that the parity of the drift wave eigenmodes is mainly

even with respect to the rational surfaces.

The ions are initially given Maxwellian velocity distributions in all three velocity directions. The parallel electron current is produced by assigning a displaced Maxwellian distribution to the electrons in the parallel velocity direction, $v_{||}$, with a drift velocity, v_d. The current is maintained in the simulations as follows. The average parallel velocity at each integration time step is computed, $\langle v_{||} \rangle = \left[\sum_{i=1}^{N_0} v_{||}(i)\right] / N_0$, with N_0 the total number of electrons. The velocity deviations with respect to the drift velocity are calculated, $\delta v_{||} = v_d - \langle v_{||} \rangle$, and added to each electron parallel velocity, $v_{||}(i)$, so that the average parallel velocity is equal to the drift velocity at all times, $\left\langle v'_{||}(i) \right\rangle = \langle v_{||}(i) + \delta v_{||} \rangle = v_d$. While this maintains the current, it does not maintain the velocity distribution or the density gradient.

Typical parameters used in the simulations are given as follows. The system lengths are $L_x \times L_y \times L_z = 64\Delta \times 32\Delta \times 6400\Delta$, with Δ being the unit grid spacing, and thirteen modes are retained in the mode expansion for the z direction, $n = 0, \pm 1, \ldots, \pm 6$. The particle sizes are $a_x = a_y = \Delta$, $a_z = 200\Delta$, and there are 16 particles per cell. The electron to ion mass ratio is $m_e/m_i = 1/100$, and the temperature ratio is $\tau = T_e/T_i = 1$. The magnetic field strength (B_0) is such that the ratio of ion cyclotron frequency (ω_{ci}) to electron plasma frequency (ω_{pe}) is $\omega_{ci}/\omega_{pe} = 0.05$. The density gradient scale length is taken to be $L_n = 14.2\Delta$ or $\kappa = 0.07$. The thermal velocity of the electron, $v_e = \left(T_e/m_e\right)^{1/2}$, is such that $v_e/\omega_{pe}\Delta = 1$, which means that the electron Debye length, λ_D, is equal to the grid spacing. The ion thermal velocity, $v_i = \left(T_i/m_i\right)^{1/2}$, is such that $v_i/v_e = 0.1$, and the sound speed, $c_s = \left(T_e/m_i\right)^{1/2}$, is then determined by $c_s/v_e = 0.1$. The Larmor radius of the ions $\left(\rho_i = v_i/\omega_{ci}\right)$ is taken to be $\rho_i/\Delta = 2.0$, while the sound Larmor radius $\left(\rho_s = c_s/\omega_{ci}\right)$ is $\rho_s/\Delta = 2.0$ or $\rho_s = \rho_i$ in this case. The electron diamagnetic drift frequency, $\omega_{*e} = k_y \kappa c T_e/eB = k_y c_s \left(\rho_s/L_n\right)$, is determined to be $\omega_{*e}/\omega_{pe} \approx 2.75 \times 10^{-3} m$, and the ion diamagnetic drift frequency is defined by $\omega_{*i} = -\omega_{*e} T_i/T_e$.

An angle, $\theta = 1°$, was chosen for the shearless cases so that $B_y/B_0 = 0.01745$. As we shall describe later, there is no threshold for the current driven drift waves in a shearless magnetic field since the universal mode is itself unstable in the absence of a drift. The angle of 1° was chosen so as to minimize the growth rate of the universal mode but still

achieve substantial growth rates in the presence of a parallel drift. In the sheared cases, the shear length (L_s) is chosen such that $L_s/L_n = 14$. This choice was made to ensure that the ion resonance layers, where ion shear damping occurs and whose locations are defined by $\omega/k_{||}v_i \approx 1$, i.e., $\omega/\left[|k_z + k_y\left(x - x_0\right)|v_i\right] \approx 1$ or $x_i - x_{mn} = \omega L_s/k_y v_i$, are within the system for $\omega \approx \omega_{*e}$. If $x_i\left(\omega_{*e}\right) < L_x$, then $x_i(\omega)$, with ω being the eigenmode frequency, will be well within the system since ω is always less than ω_{*e}. This condition also determines L_z, since all x_i's centered about the various x_{mn}'s should be within the system.

The simulations have been run up to $\omega_{ci}t = 200$ or $\omega_{*e}t \approx 10$ (for $k_y\rho_s = 0.392$) with a time step of $\omega_{pe}\Delta t = 2$.

III. Linear Theory

In this section, we briefly review the linear theory of current driven drift waves.

The governing equation[5] for potential fluctuations of the form $\phi = \phi(x)\exp\left[i\left(k_y y - \omega t\right)\right]$, with magnetic field $\vec{B} = B_0\left(\hat{z} + \hat{y}x/L_s\right)$, and parallel wave number $k_{||} = k_y x/L_s$, can be written as

$$\left[\rho_s^2\frac{d^2}{dx^2} + Q(x,\omega)\right]\phi(x) = 0. \tag{1}$$

The potential, Q, is expressed as

$$Q = \frac{(1+\tau)\frac{\omega}{\omega_{*e}} + \xi_i Z(\xi_i)\left(1+\tau\frac{\omega}{\omega_{*e}}\right)\Gamma_0 + \left(\frac{\omega'}{\omega_{*e}} - 1\right)\xi_e Z\left(\xi_e'\right)}{\xi_i Z(\xi_i)\left(\frac{\omega}{\omega_{*e}} + \frac{1}{\tau}\right)\left(\Gamma_0 - \Gamma_1\right)}, \tag{2}$$

where $\xi_{e,i} = \omega/\sqrt{2}\left|k_{||}\right|v_{e,i}$, $\omega' = \omega - k_{||}v_d$, $\xi_e' = \omega'/\sqrt{2}\left|k_{||}\right|v_e$, $b = \left(k_y\rho_i\right)^2$, $\Gamma_n = I_n(b)e^{-b}$ with I_n, a modified Bessel function, and Z is the plasma dispersion function.

The eigenmode equation, Eq. (1), is equally applicable to two- and three-dimensional sheared, slab configurations. In 3D, it applies to each rational surface position, x_{mn}. The x dependence of the parallel wave number, $k_{||}(x)$, for the sheared case, tends to localize the eigenfunctions about their respective mode rational surfaces, x_{mn}.

The dispersion relation of current driven drift waves in the absence of shear is obtained by setting the numerator of Q, Eq. (2), equal to zero,

$$(1+\tau)\frac{\omega}{\omega_{*e}} + \xi_i Z(\xi_i)\left(1+\tau\frac{\omega}{\omega_{*e}}\right)\Gamma_0 + \left(\frac{\omega'}{\omega_{*e}} - 1\right)\xi_e Z\left(\xi_e'\right) = 0. \tag{3}$$

Here, $k_{\|} = k_z + k_y \sin\theta$ with θ constant, and $b = \left(k_x^2 + k_y^2\right)\rho_i^2$. The dispersion relation for the shearless current driven drift wave, Eq. (3), is solved for the shearless slab parameters of the simulations described in Sec. II. Figure 2 illustrates the variation of the growth rate, γ, and frequency, ω, (normalized to ω_{ci}) as the drift velocity, v_d/c_s, increases from 0 to 12. Three values of $k_y\rho_i$ (0.196, 0.392, and 0.588) are represented, and $\theta = 1°$. The growth rate increases approximately linearly with v_d/c_s; we note that γ is finite even for $v_d = 0$, and that $\gamma > \omega$ for $v_d/c_s \geq 6$. Finite k_z ($k_z = 2\pi n/6400$) slightly alters the growth rates of Fig. 2, and for the parameters chosen, all k_z modes will grow at the growth rate of the particular $k_y\rho_i$ mode.

The inhomogeneous eigenmode equation for the sheared current driven drift wave, Eq. (1), is solved for the sheared slab parameters of Sec. II using the Gladd-Horton[4] and Ross-Mahajan[5] shooting code. Growth rates, γ, and real frequencies, ω, (normalized to ω_{*e}) as a function of v_d/c_s are displayed in Fig. 3, for the same $k_y\rho_i$ values presented in Fig. 2. Similar to the result of the shearless case, γ increases roughly linearly with v_d/c_s beyond the instability threshold. As already noted by Gladd and Liu,[6] the threshold drift velocity at $v_d/c_s = 2.5$ is almost independent of wave number and agrees well with the Rosenbluth-Liu[11] threshold estimate,

$$\left(v_d/c_s\right)_{\text{Thres.}} = \left(\frac{8}{\pi}\right)^{1/2}\left(\frac{L_n}{L_s}\right)\left(1+\frac{T_i}{T_e}\right)\left(\frac{m_i}{m_e}\right)^{1/2}, \tag{4}$$

which yields $\left(v_d/c_s\right)_{\text{Thres.}} \approx 2.3$ for our parameters. A typical eigenmode is illustrated in Fig. 4b for $v_d/c_s = 10$ ($\omega/\omega_{*e} = 0.490$, $\gamma/\omega_{*e} = 0.636$, $k_y\rho_i = 0.392$). We note that the eigenmode is shifted away from the rational surface as compared to the stable universal mode case, Fig. 4a, so that the symmetry with respect to x_0 has been broken by the parallel electron drift.

IV. Shearless Field Results

Both 2D and 3D results, for the case of a shearless magnetic field with $\theta = 1°$, are presented in this section. The parameters described in Sec. II are used, and the current is maintained throughout the simulations.

Typical results from a 2D run with $v_d/c_s = 6$ are displayed in Figs. 5, 6, 7, and 8. For our configuration, a negative drift gives instability. Figure 5 depicts the time history of: a) parallel electron and ion temperatures; b) perpendicular ion temperatures; and c) total electrostatic field energy. The exponential increase of the field energy, up to saturation at $\omega_{ci}t = 200$, is accompanied by a 30% increase of the parallel electron temperature and a lesser increase (3–4%) of the ion temperature. Snapshots of the parallel electron distribution function (Fig. 6a) at $\omega_{ci}t = 0$ and $\omega_{ci}t = 200$ show steepening of the distribution around $v_{||} = v_d$ and a corresponding broadening at saturation. The potential structure as a function of x for the most unstable mode ($k_y\rho_i = 0.392$) is plotted in Fig. 6b. The wave form is closely fitted by $\sin(2\pi x/L_x)$ as expected from the mode structure allowed with $\phi = 0$ boundary conditions. Density and parallel temperature profiles are displayed in Figs. 7a, b, c, and d at the initial time ($\omega_{ci}t = 0$), and at saturation ($\omega_{ci}t = 200$). Definite flattening of the density profile occurs, which is greater for the electrons than the ions. Global electron heating (i.e., at all points in x) accompanies the flattening of the density profile and saturation of the electrostatic energy.

A composite plot for the characteristics of the most unstable potential fluctuation mode, $k_y\rho_i = 0.392$ or the fundamental mode in our $L_y = 32\Delta = 16\rho_s$ system, is presented in Fig. 8. The second mode ($k_y\rho_s = 0.784$) shows a much smaller growth, and all other fluctuations are found to be stable. The time evolution of the real and imaginary parts of the potential fluctuation, when frequencies other than $-\omega_{ci} < \omega < \omega_{ci}$ have been filtered out, is displayed in Fig. 8a. Figure 8b shows the time evolution of the amplitude of the same low frequency part of $e\phi/T_e$. Oscillating exponential growth of the potential fluctuation, up to saturation at $\omega_{ci}t = 200$, indicates a measured growth rate of $\gamma/\omega_{ci} = 0.3$, and a frequency of $\omega/\omega_{ci} = 0.35$, which are both in agreement with the linear theory results ($\gamma/\omega_{ci} = 0.37$ and $\omega/\omega_{ci} = 0.32$). This is confirmed by a potential fluctuation power spectrum, averaged over all x, which is shown in Fig. 8c. Note the slight upshift in

frequency of the nonlinear phase ($\omega_{ci}t > 100$) from the less well resolved (hence the broader peak) linear phase ($\omega_{ci}t < 100$). The theoretical frequency, indicated by an arrow along the frequency axis, coincides with the simulation peaks.

Similar results are obtained for other drift velocities, $1 < v_d/c_s < 12$. A plot of the measured real frequencies and growth rates compared to theoretical predictions for the mode $k_y\rho_i = 0.392$, as a function of v_d/c_s, is shown in Fig. 9a. Good agreement between theory and simulation is apparent. The saturation amplitude of this most unstable mode, as a function of v_d/c_s, is illustrated in Fig. 9b. The level increases with v_d/c_s, for $\gamma < \omega$, but tapers off for v_d/c_s values such that $\gamma > \omega$.

We have determined that saturation is accompanied not only by a flattening of the density profile but also by a modification of the space average distribution function at saturation. Considerable electron heating also occurs when the instability saturates. This suggests that saturation occurs by quasilinear plateauing of the electron distribution function, which is the free energy source. Here, current diffusion[9] is precluded since the current is maintained throughout the simulation. The plateauing is dramatically illustrated in Fig. 10 where three-dimensional constructions of $f_e\left(x, v_{||}\right)$ are displayed at an early time ($\omega_{ci}t = 40$) and during the steady state ($\omega_{ci}t = 200$). We note the flattening in both x and $v_{||}$. This diagnostic[12] is one of the main motivational bases for the quasilinear plateau theory presented in Sec. VI.

One 3D simulation has also been performed using the same parameters of the 2D simulation presented in detail in Figs. 5–10 (i.e., $v_d/c_s = 6$), but with a set of $k_z = 2\pi n/L_z$ modes, $n = 0, \pm 1, \ldots, \pm 4$. The features of the run are very similar to the 2D case and will not be repeated here. It is, however, worth showing snapshots of the electron and ion density and temperature profiles at $\omega_{ci}t = 0$ and at saturation. This is presented in Fig. 11. The density profiles have been completely flattened, and the electron temperature increases more in what was the high density side initially. Figure 12 displays the time evolution of the amplitudes for various unstable modes in the simulation. From linear theory, we again expect modes with $k_y\rho_s = 0.392$ to be most unstable. Indeed, many (m, n) pairs grow with comparable growth rate for the same $m = 1$ values, as expected from linear theory since $k_z \ll k_y \sin\theta$ so that $k_{||}$ is still determined primarily by k_y. All (m, n) pairs achieve a

lower saturation level than the corresponding unstable $m = 1$, $n = 0$ mode in the 2D case. It is clear that more modes grow at the expense of the same free energy. The saturation mechanism is again identified as plateauing of the electron distribution function in x and $v_{\|}$.

V. Sheared Field Results

Both 2D and 3D results, for the case of a sheared magnetic field with $L_s/L_n = 14$, are presented in this section. The parameters described in Sec. II are used, and rational surfaces are located about $x_0 = L_x/2$.

Typical results from a 2D run with $v_d/c_s = 10$ are displayed in Figs. 13, 14, 15, 16, and 17. For our configuration, a positive drift gives instability with the mode localized up the gradient, (i.e., on the high density side). Figure 13 depicts the time histories of: a) parallel electron and ion temperatures; b) perpendicular ion temperature; and c) total electrostatic field energy. As found in the shearless case, parallel electron heating accompanies growth and saturation (at $\omega_{ci}t \approx 120$) of the total electrostatic energy. Snapshots of the electron distribution function (Fig. 14a) show some heating at $\omega_{ci}t = 120$, but less distortion is found than in the shearless case of Fig. 6a. The spatial structure of the potential fluctuations at saturation displayed in Fig. 14b shows a shift away from the rational surface up the density gradient. This spatial structure is in qualitative agreement with the linear theory, an example of which is shown in Fig. 4. Snapshots of the electron and ion density and temperature profiles (Fig. 15) show local flattening of the electron density in the spatial region of maximum mode amplitude, which is up the gradient about the rational surface. Less density distortion is apparent for the ions. The electrons are heated only up the gradient from the mode rational surface. However, the region of weaker ion heating coincides approximately with the position of maximum mode amplitude.

The behavior of the most unstable mode, the potential fluctuation with $k_y\rho_i = 0.392$, is detailed in Fig. 16. As stated in the previous section, fluctuations with frequencies other than $-\omega_{ci} < \omega < \omega_{ci}$ have been filtered out of the data. Exponential growth occurs up to $\omega_{ci}t = 100$, and saturation of the mode thereafter is clear from Figs. 16a and b. The measured growth rate, $\gamma/\omega_{*e} = 0.66$, is in agreement with the linear theory shown

in Fig. 3, which indicates that $\gamma/\omega_{*e} = 0.63$. The frequency spectrum of the fluctuation for $k_y\rho_i = 0.392$ is shown in Fig. 16c. Note the upshift of the measured frequency (to $\omega/\omega_{*e} \approx 1.5$) from the predicted linear eigenmode frequency indicated by an arrow on the frequency axis (at $\omega/\omega_{*e} = 0.49$), which is a direct consequence of local profile flattening and local heating.

An interferogram of the fluctuation with $k_y\rho_i = 0.392$ is performed as follows.[13] The correlation of the fluctuation, $\phi_{k_y}(x,t)$, with a reference signal, $\sin(\omega_0 t)$, over the interval 0 to T, is calculated as $I_{k_y}(x,\omega_0) = \frac{1}{T}\int_0^T dt\phi_{k_y}(x,t)\sin(\omega_0 t)$. The resulting eigenmode structure obtained with $\omega_0/\omega_{*e} = 0.49$ is plotted in Fig. 17 against the shooting code prediction for $v_d/c_s = 10$. There is qualitative agreement in terms of the overall eigenmode shape and the extent of the shift away from the rational surface.

Similar results have been obtained for other drift velocities, $3 < v_d/c_s < 12$. Figure 18 shows composite plots of the simulation growth rates, γ/ω_{*e} (triangles), versus theoretical ones (dashed curve) as a function of v_d/c_s, for the fluctuation with $k_y\rho_i = 0.392$. The agreement is good between simulation and theory. The variation of the saturation level of this particular mode with v_d/c_s is illustrated in Fig. 19a. The filled in circles are simulation results when the current is maintained. The open circles are results for cases when the current is not maintained. In both cases the saturation levels are comparable, which indicates that current diffusion is not the major factor in the saturation. One additional case for a system size of $L_y = 64\Delta$ (with current maintained) is identified in Fig. 19a by a triangle. For this multi-mode case, the $k_y\rho_i = 0.392$ fluctuation corresponds to the second mode of the twice elongated system. The saturation level is slightly lower because at least three modes are unstable in this situation, as shown in Fig. 3. It is clear from Fig. 19a that the potential saturation level increases approximately linearly with v_d/c_s. Figure 19b shows the variation of the saturation level with mode number for these three unstable modes. The saturation is roughly proportional to k^{-1}.

For the simulation with shear, one might think that density profile flattening dominates over electron distribution function modifications, since the space-averaged distribution function of Fig. 14 shows little distortion from its original Maxwellian shape. Three-dimensional constructions of $f_e\left(x, v_{||}\right)$ displayed in Fig. 20 do, however, show local

hollowing of the distribution in both x and $v_{||}$ about the rational surface in the steady state. Again, saturation is caused by modification of $f_e\left(x, v_{||}\right)$ by the unstable modes. In Sec. VI, a quasilinear theory of this phenomenon and the saturation levels obtained from it are compared to the simulation results.

One 3D simulation with a sheared magnetic field has been performed with the following parameters: $v_d/c_s = 10$, and $k_z = 2\pi n/L_z$; $n = 0, \pm 1, \ldots, \pm 6$ with $L_z = 6400\Delta$, so that again $k_z \ll k_y$. The other parameters are identical to those described in Sec. II. The overall behavior of the plasma is similar to the 2D cases. There is somewhat more density profile flattening and more electron heating. The major difference resides in the number of modes that are growing. Many (m, n) pairs with $m = 1$ (corresponding to the most unstable mode in 2D) are excited as is evident from Fig. 21 where potential contours for various ($m = 1$, n) pairs are displayed in an $x - y$ plot. Time evolutions of the potential fluctuations for several ($m = 1$, n) pairs are presented in Fig. 22. The linear growth rates of the modes with different k_z's are not identical, as might be expected from linear theory. Evidently, nonlinear effects are present, either due to the stochastic[14] behavior of the electrons in the presence of multiple rational surfaces or due to n-mode coupling of the potential fluctuations. Nevertheless, our diagnostics show that saturation is again accompanied by density profile flattening and hollowing of the parallel electron distribution function in both x and $v_{||}$ as in the previous cases. In fact, test particle trajectory diagnostics are presented in Sec. VI which demonstrate that the electron orbits follow the diffusion paths of the quasilinear plateau theory rather than exhibiting stochastic behavior, as found for the marginally unstable 3D drift waves.[15] The dominance of the quasilinear diffusion orbits over a stochastic character is understood by noting that the stochastic correlation frequency, ω_c, is much less than the large current driven drift wave growth rate, γ. Consequently, the distribution function is plowed before the electrons are able to behave stochastically.

VI. Quasilinear Plateau Theory

A quasilinear plateau (QLP) theory[16,17] is based on the argument that one can calculate the saturated state by assuming that the final distribution contours, in the resonance region, are parallel to the diffusion paths. In this theory, the diffusion paths have been created by excited waves in the plasma. The analysis proceeds by deriving a quasilinear diffusion equation which describes the alteration of the initial distribution function due to linear unstable modes in the system. The particles which are in resonance with the waves are diffused until the initial gradients in the distribution function are flattened to the point of a plateau formation, such that no more alteration can occur. In this steady state, the final distribution contours are parallel to the diffusion paths in the resonance region. Using the above QLP argument, one can compute the final distribution function at saturation as well as the final amplitude of the waves in the plasma. In this calculation, the loss in resonant particle energy is equated with the gain in wave energy.

The quasilinear diffusion equation, which governs the alteration of the initial distribution function, is derived by combining the linear response due to waves with the average distribution function equation. After a random phase approximation (RPA)[16,18] is invoked while averaging the quadratic potential fluctuation term, the resultant quasilinear diffusion equation for electrons is

$$\frac{\partial f_e\left(x,v_{\|},t\right)}{\partial t}=\sum_{\vec{k}}\left(-\frac{e}{m_e}k_{\|}\frac{\partial}{\partial v_{\|}}+\frac{c}{B}k_y\frac{\partial}{\partial x}\right)\frac{\gamma_{\vec{k}}\left|\phi_{\vec{k}}\right|^2}{\left(\omega_{\vec{k}}-k_{\|}v_{\|}\right)^2+\gamma_{\vec{k}}^2} \times\left(-\frac{e}{m_e}k_{\|}\frac{\partial}{\partial v_{\|}}+\frac{c}{B}k_y\frac{\partial}{\partial x}\right)f_e\left(x,v_{\|},t\right). \tag{5}$$

Here, an expansion using the linear eigenfunctions, $\epsilon_{\vec{k},\omega}\phi_{\vec{k}}=0$, is employed, where the complex eigenfrequency is $\omega=\omega_{\vec{k}}+i\gamma_{\vec{k}}$. The initial current driven electron distribution with an exponential density gradient is

$$f_e^0=A\exp\left[-\left(\frac{x}{L_n}\right)-\left(\frac{v_{\|}-v_d}{\sqrt{2}v_e}\right)^2\right],\quad A=\frac{V}{\sqrt{2\pi}v_eL_n\left[1-\exp\left(-L_x/L_n\right)\right]}, \tag{6}$$

where $N_0=n_0V$, and n_0 is the number density. The steady state, or QLP, occurs when the contours of the evolved distribution are parallel to the two-dimensional diffusion paths

in $(x, v_{||})$ space,

$$\left(-\frac{e}{m_e}k_{||}\frac{\partial}{\partial v_{||}} + \frac{c}{B}k_y\frac{\partial}{\partial x}\right) f_e\left(x, v_{||}, t_{\text{final}}\right) = 0. \tag{7}$$

In the following two subsections, the shearless and sheared configurations will be examined, and the final saturation wave amplitudes calculated. All further distributions are assumed to be that of the electrons which give the dominant energy change contribution.

A. Shearless

The final amplitude of the linearly unstable current driven drift wave is calculated by determining the energy loss which occurs when the initial distribution is transformed into the final QLP distribution. In order to derive an expression for the change in particle energy, it is necessary to obtain the initial contour slope,

$$m_C = \frac{dx}{dv_{||}} = -\frac{\sqrt{2}L_n}{v_e}\left(\frac{v_{||}}{\sqrt{2}v_e} - \frac{v_d}{\sqrt{2}v_e}\right), \tag{8}$$

and the final diffusion path slope,

$$m_D = \frac{dx}{dv_{||}} = -\frac{\sqrt{2}L_n}{v_e}\left(\frac{\omega_{*e}}{\sqrt{2}k_{||}v_e}\right). \tag{9}$$

As depicted in Fig. 23a, electrons which diffuse to a lower phase space density also scatter to a lower velocity, since the initial contour slope is greater than the diffusion path slope, $m_C > m_D$, in the "resonant" region where $\left(\omega_{\vec{k}} - \gamma_{\vec{k}}\right)/k_{||} \lesssim v_{||} \lesssim \left(\omega_{\vec{k}} + \gamma_{\vec{k}}\right)/k_{||}$. This process results in particle energy loss in the "resonant" region so that the wave energy increases up to a final field amplitude at saturation, $\left(e\phi/T_e\right)_{\text{sat.}}$. The final QLP state is presented in Fig. 23b, where the distribution, in the "resonant" region, has evolved to a state in which the contour lines are parallel to the diffusion lines, $m_C \rightarrow m_D$. If a shearless magnetic field configuration is assumed, it is clear that the initial contour slope, m_C, and final diffusion path slope, m_D, are both independent of the radial dimension, x. This approximation leads to a particularly simple calculation for the saturation amplitude which can be obtained analytically. This calculation is in contrast to the sheared case which necessitates a complicated numerical solution, as presented in the following subsection.

The change in the distribution function from initial to QLP formation is given by

$$\Delta f\left(x, v_{||}\right) = \left\{1 - \exp\left[-\Delta x(v_{||})/L_n\right]\right\} f^0\left(x, v_{||}\right), \tag{10}$$

where the radial change is

$$\Delta x(v) = \Delta x_1 + m_D(v - v_1) - \int_{v_1}^{v} dv' m_c(v'), \quad \Delta x_1 = x_1' - x_1. \tag{11}$$

In order to determine the precise change in distribution, it is necessary to invoke a conservation of particle constraint,

$$\int dx \int_{v_1}^{v_2} dv_{\|} n_0 \Delta f\left(x, v_{\|}\right) = \int_{v_1}^{v_2} dv_{\|} n_0 \Delta f(v_{\|}) = 0. \tag{12}$$

This final expression closes the set of equations which determines the change in distribution function $\Delta f(v_{\|})$ or Δx_1.

The saturation amplitude is obtained using the energy balance equation,

$$\frac{\partial}{\partial t}\left(\int d\vec{x}\, TWED\right) = -\frac{\partial}{\partial t}\left(\int d\vec{x}\, RPKED\right), \tag{13}$$

between the change in total wave energy,

$$\Delta\left(\int d\vec{x}\, TWED\right) \approx V \frac{k^2}{8\pi} \mathrm{Re}\left(\omega_{\vec{k}} \frac{\partial \epsilon_{\vec{k},\omega_{\vec{k}}}}{\partial \omega_{\vec{k}}}\right) \left|\phi_{\vec{k}}\right|^2, \tag{14}$$

and the change in resonant particle energy,

$$\Delta\left(\int d\vec{x}\, RPKED\right) \approx V \int_{v_1}^{v_2} dv_{\|} \frac{1}{2} m_e n_0 v_{\|}^2 \Delta f(v_{\|}). \tag{15}$$

Combining Eqs. (13), (14), and (15), the saturation potential amplitude is

$$\left(\frac{e\phi}{T_e}\right)_{\text{sat.}} = \left[\frac{-\int_{v_1}^{v_2} dv_{\|} \left(\frac{v_{\|}}{v_e}\right)^2 \Delta f(v_{\|})}{(k\lambda_D)^2 \,\mathrm{Re}\left(\omega_{\vec{k}} \frac{\partial \epsilon_{\vec{k},\omega_{\vec{k}}}}{\partial \omega_{\vec{k}}}\right)}\right]^{1/2}, \tag{16}$$

where the dielectric term is given by

$$\begin{aligned}(k\lambda_D)^2 \omega \frac{\partial \epsilon_{\vec{k},\omega}}{\partial \omega} = {} & \tau \xi_i Z(\xi_i) \Gamma_0 - 2\Gamma_0 \left(\tau \xi_i + \frac{\omega_{*e}}{\omega} \xi_i\right) \xi_i \left[1 + \xi_i Z(\xi_i)\right] \\ & + \xi_e Z(\xi_e') - 2\left(\xi_e' - \frac{\omega_{*e}}{\omega} \xi_e\right) \xi_e \left[1 + \xi_e' Z(\xi_e')\right].\end{aligned} \tag{17}$$

Using the change in distribution function, Eq. (10), for the evaluation of Eq. (16), the final expression for the saturation amplitude is

$$\left(\frac{e\phi}{T_e}\right)_{\text{sat.}} = \left\{ \frac{\frac{2}{\sqrt{\pi}} \int_{u_1-u_d}^{u_2-u_d} dy e^{-y^2}}{\left(k\lambda_D\right)^2 \text{Re}\left(\omega_{\vec{k}} \frac{\partial \epsilon_{\vec{k},\omega_{\vec{k}}}}{\partial \omega_{\vec{k}}}\right)} \right.$$

$$\left. \times \left[\frac{\frac{1}{2} \int_{\sqrt{2}(u_1-R/2-u_d)}^{\sqrt{2}(u_2-R/2-u_d)} dy \left(y + R/\sqrt{2} + \sqrt{2}u_d\right)^2 e^{-y^2}}{\int_{\sqrt{2}(u_1-R/2-u_d)}^{\sqrt{2}(u_2-R/2-u_d)} dy e^{-y^2}} - \frac{\int_{u_1-u_d}^{u_2-u_d} dy \left(y+u_d\right)^2 e^{-y^2}}{\int_{u_1-u_d}^{u_2-u_d} dy e^{-y^2}} \right] \right\}^{1/2} . \tag{18}$$

Here, $R = \omega_{*e}/\sqrt{2}k_{\|}v_e$, and the normalized velocities are: $u_d = v_d/\sqrt{2}v_e$; $u_1 = \left(\omega_{\vec{k}} - \gamma_{\vec{k}}\right)/\sqrt{2}v_e k_{\|}$; and $u_2 = \left(\omega_{\vec{k}} + \gamma_{\vec{k}}\right)/\sqrt{2}v_e k_{\|}$. The expression for the saturation potential, Eq. (18), can be approximately evaluated for $\left(k\lambda_D\right)^2 \omega \frac{\partial \epsilon}{\partial \omega} \approx 1$ and $\omega_{\vec{k}}/k_{\|}v_e \approx u_d$,

$$\left(\frac{e\phi}{T_e}\right)_{\text{sat.}} \approx .2 \left\{ \frac{2\sqrt{2}}{\sqrt{\pi}} \left[\left(\frac{L_s}{L_n}\right)^2 \frac{m_e}{2m_i} \right] \frac{\gamma_{\vec{k}}}{\omega_{*e}} \frac{v_d}{v_e} \right\}^{1/2} . \tag{19}$$

The full expression for the saturation potential, Eq. (18), is evaluated and compared to the simulation values. The comparison is presented in Fig. 24. The QLP theory is seen to be in good agreement with the simulation for the shearless configuration.

B. Sheared

The analysis of the current driven drift wave saturation state presented in this section, using a QLP theory for one rational surface in a sheared slab, is used to compare with simulation and proposed as a model of reality. As was mentioned previously, the electrons are expected to follow QLP trajectories instead of stochastic orbits, even for the general multirational surface case. This electron behavior can be understood by comparing the stochastic correlation rate,

$$\omega_c = \left(\frac{2k_y^2 v_e^2 D}{3L_s^2} \right)^{1/3} ,$$

to the current driven growth rate, γ. Here, the diffusion coefficient is calculated from

$$D = \sum_{m,n} \frac{c}{B} k_y^2 \left|\phi_{mn}\right|^2 \pi \delta\left(\omega - k_{\|}v_e\right) \rightarrow \sqrt{\frac{T_i}{T_e}\frac{m_e}{m_i}} \frac{c_s^2}{\omega} \left(\frac{e\phi}{T_e}\right)^2 \left(k_y\rho_s\right)^2 .$$

For the test case of $v_d/c_s = 10$ the ratio of growth rate to correlation rate is $\gamma/\omega_c \approx 3$. It is clear that the distribution function will be severely plowed before stochastic dynamics

come into play, and the particle trajectories will tend to follow the quasilinear diffusion paths as demonstrated at the end of this section.

The QLP theory applied to a sheared configuration is greatly complicated by the fact that the diffusion path,

$$u_d = C - \frac{\rho_s}{4L_n R}\mathbf{X}^2, \quad \text{for} \quad m_D = \frac{-2R\left(L_n/\rho_s\right)}{\mathbf{X}}, \tag{20}$$

is now a function of radial position. Here, $R = \omega_{*e}\Big/\left(\sqrt{2}v_e k'_{\|}\rho_s\right) = \left(m_e/2m_i\right)^{1/2} L_s/L_n$, the normalized position is $\mathbf{X} = (x - x_0)/\rho_s$, and the normalized velocity is $u = v_{\|}/\sqrt{2}v_e$. The diffusion path is a parabola centered about the mode rational radial surface where the parameter, C, is an arbitrary variable defining a particular diffusion path, as depicted in Fig. 25. The initial contour lines,

$$\mathbf{X} = C' - \frac{L_n}{\rho_s}\left(u_C - u_d\right)^2, \quad \text{for} \quad m_C = -2\frac{L_n}{\rho_s}\left(u - u_d\right), \tag{21}$$

and the resonant boundaries,

$$\left(\Omega - \frac{u\mathbf{X}}{R}\right)^2 = \Gamma^2, \quad \text{or} \quad u_R^{1,2} = R\frac{\Omega \pm \Gamma}{\mathbf{X}}, \tag{22}$$

are also depicted in Fig. 25. Here, the normalized frequency, $\Omega = \omega_{\vec{k}}/\omega_{*e}$, and growth rate, $\Gamma = \gamma_{\vec{k}}/\omega_{*e}$, has been used. As described in the previous section, in order to calculate the final potential at saturation, the change in particle energy is related to the change in wave energy. A subsidiary particle conservation constraint is imposed which allows a determination of the final altered distribution function in the "resonant" region.

In order to calculate the change in resonant particle energy, it is convenient to change variables from rectangular (velocity)-(radial) variables, $u - \mathbf{X}$, to (along-diffusion-path)-(radial) variables, $C - \mathbf{X}$. The two-dimensional $(u, \mathbf{X})$ integrals transform as

$$\int du \int d\mathbf{X}[\,] = \int dC \int_{\mathbf{X}^-(C)}^{\mathbf{X}^+(C)} d\mathbf{X} J[\,]\Big|_{u=u_D}, \quad J = \text{Jacobian} = 1, \tag{23}$$

where the intersection between diffusion path and resonant boundaries are given by the roots of

$$\left(\mathbf{X}^{\pm}\right)^3 - C\left(4\frac{L_n}{\rho_s}R\right)\mathbf{X}^{\pm} + \left(4\frac{L_n}{\rho_s}R\right)R(\Omega \pm \Gamma) = 0. \tag{24}$$

The change in resonant particle energy is then given by

$$\Delta E = m_e n_0 v_e^2 \left(\sqrt{2} v_e \rho_s\right) \int dC \int_{\mathbf{X}^-(C)}^{\mathbf{X}^+(C)} d\mathbf{X} \left(C - \frac{\rho_s}{4L_n R}\mathbf{X}^2\right)^2 \Delta f(\mathbf{X}, C), \qquad (25)$$

where the change in distribution function is

$$\begin{aligned}\Delta f(\mathbf{X}, C) &= f_{\text{sat.}} - f^0 \\ &= A\left\{F(C) - \exp\left[-\frac{\rho_s}{L_n}\left(\mathbf{X} + \frac{L_x}{2\rho_s}\right) - \left(C - \frac{\rho_s}{4L_n R}\mathbf{X}^2 - u_d\right)^2\right]\right\}. \end{aligned} \qquad (26)$$

In the evaluation of the energy change, Eq. (25), it is necessary to determine the new distribution contour parameter, $F(C)$, at each integration step (or for each particular value of the contour parameter, C). This is achieved by using the particle conservation constraint which results in solving the integral equation

$$\int_{\mathbf{X}^-(C)}^{\mathbf{X}^+(C)} d\mathbf{X}\left\{F(C) - \exp\left[-\frac{\rho_s}{L_n}\left(\mathbf{X} + \frac{L_x}{2\rho_s}\right) - \left(C - \frac{\rho_s}{4L_n R}\mathbf{X}^2 - u_d\right)^2\right]\right\} = 0, \qquad (27)$$

for each value of C.

The final equation for the saturation potential is obtained through the use of the energy conservation equation (Eq. 13),

$$\left(\frac{e\phi}{T_e}\right)_{\text{sat.}} = \left\{\frac{-\left(\rho_s/L_n\right) 2I}{\sqrt{\pi}\left[1 - \exp\left(L_x/L_n\right)\right]\left[\dfrac{\text{Re}\int dx \hat{\phi}^*(x)\left[(k\lambda_D)^2 \omega_{\vec{k}} \frac{\partial \epsilon_{\vec{k},\omega_{\vec{k}}}}{\partial \omega_{\vec{k}}}\right]\hat{\phi}(x)}{\int d\vec{x}\left|\hat{\phi}(x)\right|^2}\right]}\right\}^{1/2}, \qquad (28)$$

where the energy integral, determined from Eq. (25), is

$$\begin{aligned} I = -\int dC \int_{\mathbf{X}^-(C)}^{\mathbf{X}^+(C)} d\mathbf{X}\left(C - \frac{\rho_s}{4L_n R}\mathbf{X}^2\right)^2 \Bigg\{F(C) - \exp\Bigg[-\frac{\rho_s}{L_n}\left(\mathbf{X} + \frac{L_x}{2\rho_s}\right) \\ - \left(C - \frac{\rho_s}{4L_n R}\mathbf{X}^2 - u_d\right)^2\Bigg]\Bigg\}, \end{aligned} \qquad (29)$$

and the normalized radial eigenfunction is defined by $\phi(x) = \phi\hat{\phi}(x)$, and $(1/L_x)\int_0^{L_x} dx \left|\hat{\phi}(x)\right|^2 = 1$. The dielectric operator in the above expression is

$$k^2\lambda_D^2\omega\frac{\partial\epsilon_{\vec{k},\omega}}{\partial\omega} = (\Gamma_0 - \Gamma_1)\left\{\xi_i Z(\xi_i) - 2\left(1+\frac{1}{\tau}\frac{\omega_{*e}}{\omega}\right)\xi_i^2\left[1+\xi_i Z(\xi_i)\right]\right\}\frac{\partial^2}{\partial x^2}$$
$$+\Gamma_0\left\{\tau\xi_i Z(\xi_i) - 2\left(\tau+\frac{\omega_{*e}}{\omega}\right)\xi_i^2\left[1+\xi_i Z(\xi_i)\right]\right\} \qquad (30)$$
$$+\xi_e Z\left(\xi_e'\right) - 2\left(\frac{\omega'}{\omega}-\frac{\omega_{*e}}{\omega}\right)\xi_e^2\left[1+\xi_e' Z\left(\xi_e'\right)\right].$$

The potential at saturation is numerically evaluated, Eq. (28), while at each step the altered distribution contour parameters are stored and the final distribution contour is plotted and compared to simulation as shown in Fig. 26. Here, the simulation configuration is such that the eigenmode is shifted down the density gradient in order to directly compare with theory. The QLP theory gives a plateau formation very similar to that of simulation, so that both hole formations in Fig. 26 are quite closely matched. The final saturation potential amplitude from the QLP theory is compared with simulation and presented in Fig. 27. There is a very close agreement between simulation and QLP theory. It should be noted that the QLP theory can be used to calculate only the difference in potential energy from initial condition to saturation. The error bars for the QLP theory calculation, depicted in Fig. 27, are due to an uncertain initial simulation value, $\left(e\phi/T_e\right)_{\text{init.}} = .02 \pm .005$. Also, the QLP theory estimates of the saturation potentials, given in Fig. 27, are indicated up to $v_d/c_s = 8$, since the theory assumptions break down for $v_d/c_s > 8$, because $\gamma_{\vec{k}} > \omega_{\vec{k}}$.

A final check between simulation and QLP theory is demonstrated by observing individual electron trajectories in the "resonance" region. Samples of exact electron trajectories, in $x - v_{||}$ space, are presented in Fig. 28. Using the data points displayed in Fig. 28d, a regression analysis is performed to fit the parabolic-type curve shown. The regression analysis is compared with the theoretical diffusion path parabola,

$$\left(\frac{v_{||}}{v_e}\right)_{\text{th.}} = K - \alpha_{\text{th.}}\left(\frac{x-x_0}{\Delta}\right)^2, \quad \alpha_{\text{th.}} = \frac{\sqrt{2}\rho_s}{4L_nR}\left(\frac{\Delta}{\rho_s}\right)^2; \quad R = \frac{L_s}{L_n}\sqrt{\frac{m_e}{2m_i}}, \qquad (31)$$

where the theoretical quadratic coefficient is $\alpha_{\text{th.}} = .0125$, $x_0 = 31$, and $K = .667$. The

least squares regression analysis reduced to

$$v(x) = K - \alpha_{\text{sim.}} (x - x_0)^2, \quad J = \sum_i [v(x_i) - v_i]^2, \quad \text{with} \quad \frac{\partial J}{\partial \alpha} = 0, \tag{32}$$

where the result is

$$\alpha_{\text{sim.}} = \frac{\sum_i (K - v_i)(x_i - x_0)^2}{\sum_i (x_i - x_0)^4} = .0119. \tag{33}$$

Consequently, the QLP theory predicts a quadratic coefficient of $\alpha_{\text{th.}} = .0125$, which is very close to the simulation coefficient, $\alpha_{\text{sim.}} = .0119$. The electrons in the simulation indeed behave as particles moving along the diffusion paths in the "resonant" region, as we assumed in the QLP theory.

VII. Summary and Discussion

Simulations using both a $2\frac{1}{2}$D and a 3D electrostatic particle code in shearless and sheared magnetic field configurations have been performed to investigate the nonlinear behavior of current driven drift waves at constant current. Good agreement between simulation and linear theory was obtained for instability thresholds, growth rates, real frequency spectra, and mode structures. The growth rate exhibits an approximate linear dependence with drift velocity, v_d. Major alterations in the $x - v_{||}$ electron distribution function occurred up to saturation, while the ions showed similar behavior but to a much lesser extent. Enhancement of the parallel electron temperature for the shearless case resulted in a 30% increase prior to saturation. The alteration of the density profiles indicated flattening in x. Plowing of the distribution function occurred globally for the shearless case and locally in x, about the skewed eigenfunctions with respect to the mode rational surfaces, for the sheared case. The potential fluctuation saturation levels increased approximately with $v_d^{1/2}$ for the shearless case and with v_d for the sheared case.

The saturated state of the current driven drift modes has been analyzed using a quasilinear plateau (QLP) theory which incorporates $x - v_{||}$ diffusion. Agreement of the steady state distribution function and saturation amplitudes is good. Individual electron trajectories are found to follow the QLP theory diffusion paths. It is noted that the electron test particle trajectories do not exhibit the stochastic behavior found in a 3D drift wave analysis. This is realized in our simulation for the large drifts under consideration, since

the time to significantly plow the initial distribution function is much shorter than the stochastic correlation time induced by these current driven drift waves.

Acknowledgements

We would like to acknowledge fruitful discussions with N. T. Gladd, C. S. Liu, and M. N. Rosenbluth during the course of the work. This work was supported by USDOE grant #DE FG05-80-ET-53088.

References

1. B. B. Kadomtsev and O. P. Pogutse, Nucl. Fusion **11**, 67 (1971).
2. W. M. Tang, Nucl. Fusion **18**, 1089 (1978).
3. P. C. Liewer, Nucl. Fusion **25**, 543 (1985).
4. N. T. Gladd and C. W. Horton Jr., Phys. Fluids **16**, 889 (1973).
5. D. W. Ross and S. M. Mahajan, Phys. Fluids **22**, 294 (1979).
6. N. T. Gladd and C. S. Liu, Phys. Fluids **22**, 1289 (1979).
7. N. T. Gladd, N. A. Krall, R. W. Moses, and A. R. Jacobson, in **Plasma Physics and Controlled Nuclear Fusion Research** (IAEA, Vienna, 1985) Vol. 2, p. 619.
8. D. W. Ross and S. M. Mahajan, Phys. Rev. Lett. **40**, 324 (1978).
9. W. W. Lee, Y. Y. Kuo, and H. Okuda, Phys. Fluids **21**, 617 (1978).
10. W. W. Lee and H. Okuda, J. Comp. Phys. **26**, 139 (1978); C. Z. Cheng and H. Okuda, J. Comp. Phys. **25**, 133 (1977).
11. M. N. Rosenbluth and C. S. Liu, Phys. Fluids **15**, 1801 (1972).
12. S. Tokuda, T. Kamimura, and H. Ito, J. Phys. Soc. Japan **48**, 1722 (1980).
13. R. D. Sydora, J. N. Leboeuf, and T. Tajima, Phys. Fluids **28**, 528 (1985).
14. S. P. Hirshman and K. Molvig, Phys. Rev. Lett. **42**, 648 (1979).
15. R. D. Sydora, J. N. Leboeuf, D. R. Thayer, P. H. Diamond, and T. Tajima, submitted to Phys. Rev. Lett..
16. T. H. Dupree, Phys. Fluids **9**, 1773 (1966).
17. R. Z. Sagdeev and A. A. Galeev, **Nonlinear Plasma Theory** (W. A. Benjamin, New York, 1969).
18. R. C. Davidson, **Methods in Nonlinear Plasma Theory** (Academic Press, New York, 1972).

Figure Captions

1. Schematic of the particle simulation configuration.
2. Linear theory result in the shearless case with $\theta = 1°$. Growth rate, γ, (dotted curve) and real frequency, ω, (full curve) for $k_y\rho_s = 0.196$, 0.392, and 0.588.
3. Linear theory result in the sheared case with $L_s/L_n = 14$. Growth rate, γ, (dotted curve) and real frequency, ω, (full curve) for $k_y\rho_s = 0.196$, 0.392, and 0.588.
4. Linear theory eigenfunctions in the sheared case with $L_s/L_n = 14$ and $k_y\rho_s = 0.392$ a) $v_d/c_s = 0$, b) $v_d/c_s = 10$.
5. 2D simulation result in the shearless case with $\theta = 1°$ and $v_d/c_s = 6$. Time evolution of a) parallel electron and ion temperature, b) perpendicular ion temperature, and c) total electrostatic energy.
6. 2D simulation result in the shearless case with $\theta = 1°$ and $v_d/c_s = 6$. a) Snapshots of the distribution function at $\omega_{ci}t = 0$ (dotted curve) and $\omega_{ci}t = 200$ (full curve). b) Potential fluctuation $e\phi_k/T_e$ for mode $k_y\rho_s = 0.392$ at $\omega_{ci}t = 200$. The full curve denotes the real part and the dotted curve the imaginary part.
7. 2D simulation result in the shearless case with $\theta = 1°$ and $v_d/c_s = 6$. Snapshots at $\omega_{ci}t = 0$ (dotted curve) and $\omega_{ci}t = 200$ (full curve) of a) electron density, b) ion density, c) parallel electron temperature, and d) parallel ion temperature profiles.
8. 2D simulation result in the shearless case with $\theta = 1°$ and $v_d/c_s = 6$. a) Time evolution of the potential fluctuation $e\phi_k/T_e$ for $k_y\rho_s = 0.392$ filtered between $-\omega_{ci} < \omega < \omega_{ci}$. The full curve represents the real part and the dotted curve the imaginary part. b) Amplitude of the potential fluctuation as a function of time. c) Power spectrum of the potential fluctuation vs. frequency. The linear frequency is indicated by an arrow on the ω axis. The dashed curve is the spectrum in the linear phase ($\omega_{ci}t < 100$) and the full curve is the spectrum beyond $\omega_{ci}t = 100$ in the nonlinear phase.
9. 2D simulation result in the shearless case with $\theta = 1°$ and $v_d/c_s = 6$. Comparison of simulation (triangles) and theory (dashed curve) growth rates, and simulation (filled circles) and theory (full curve) real frequencies for the mode $k_y\rho_s = 0.392$. b) Saturation level (circles with error bars) vs. v_d/c_s for the most unstable mode with

$k_y\rho_s = 0.392$.

10. 2D simulation result in the shearless case with $\theta = 1°$ and $v_d/c_s = 6$. Three-dimensional construction of the electron distribution function $f(x, v_{||})$ at a) $\omega_{ci}t = 40$ and b) $\omega_{ci}t = 200$. Plateauing of the distribution function in both x and $v_{||}$ is apparent.

11. 3D simulation results in the shearless case with $\theta = 1°$, $v_d/c_s = 6$, and $k_z = 2\pi n/L_z$; $n = 0, \pm 1, \ldots, \pm 4$. Snapshots of a) electron density profile, b) ion density profile, c) parallel electron temperature, and d) parallel ion temperature at $\omega_{ci}t = 0$ (dotted curve) and $\omega_{ci}t = 200$ (full curve).

12. 3D simulation results in the shearless case with $\theta = 1°$, $v_d/c_s = 6$, and $k_z = 2\pi n/L_z$; $n = 0, \pm 1, \ldots, \pm 4$. Time evolution of the amplitude of the potential fluctuation $e\phi_{mn}/T_e$ for $(m, n) = (\pm 1, 0)$, $(m, n) = (-1, 1)$, $(m, n) = (-1, 2)$, $(m, n) = (-1, 3)$.

13. 2D simulation results in the sheared case with $L_s/L_n = 14$ and $v_d/c_s = 10$. Time evolution of a) parallel electron (full curve) and parallel ion (dotted curve) temperature, b) perpendicular ion temperature, and c) total electrostatic energy.

14. 2D simulation results in the sheared case with $L_s/L_n = 14$ and $v_d/c_s = 10$. a) Snapshots of the distribution function at $\omega_{ci}t = 0$ (dashed curve) and $\omega_{ci}t = 120$ (full curve). The initial drift velocity is indicated by an arrow. b) Potential fluctuation $e\phi_k/T_e$ for mode $k_y\rho_s = 0.392$ at $\omega_{ci}t = 120$. The full curve denotes the real part and the dotted curve the imaginary part.

15. 2D simulation results in the sheared case with $L_s/L_n = 14$ and $v_d/c_s = 10$. Snapshots at $\omega_{ci}t = 0$ (dotted curve) and $\omega_{ci}t = 120$ (full curve) of a) electron density, b) ion density, c) parallel electron temperature, and d) parallel ion temperature profiles.

16. 2D simulation results in the sheared case with $L_s/L_n = 14$ and $v_d/c_s = 10$. a) Time evolution of the potential fluctuation $e\phi_k/T_e$ for $k_y\rho_s = 0.392$ filtered between $-\omega_{ci} < \omega < \omega_{ci}$. The full curve represents the real part and the dotted curve the imaginary part. b) Amplitude of the potential fluctuation as a function of time. c) Power spectrum of the potential fluctuation vs. frequency. The linear frequency is indicated by an arrow on the ω axis.

17. 2D simulation results in the sheared case with $L_s/L_n = 14$ and $v_d/c_s = 10$. Compar-

ison between the real (full curves) and imaginary (dotted and dashed curves) parts of the simulation and theory eigenfunctions vs. x.

18. 2D simulation results in the sheared case with $L_s/L_n = 14$ and $v_d/c_s = 10$. Comparison of the simulation (triangles) and theory (dashed curve) growth rates for $k_y\rho_s = 0.392$.
19. 2D simulation results in the sheared case with $L_s/L_n = 14$ and $v_d/c_s = 10$. a) Saturation level of the fluctuation amplitude versus v_d/c_s for a single mode case with current maintained (filled circle—$k_y\rho_s = 0.392$), single mode case with current not maintained (crossed circle—$k_y\rho_s = 0.392$), and a multi-mode case with current maintained (triangle—$k_y\rho_s = 0.392$). b) Saturation amplitude vs. $k_y\rho_s$, for $v_d/c_s = 12$.
20. 2D simulation results in the sheared case with $L_s/L_n = 14$ and $v_d/c_s = 10$. Three-dimensional construction of the electron distribution function $f(x, v_{||})$ at a) $\omega_{ci}t = 40$ and b) $\omega_{ci}t = 200$. Plateauing of the distribution function in both x and $v_{||}$ is apparent.
21. 3D simulation results in the sheared case with $L_s/L_n = 14$, $v_d/c_s = 10$, and $k_z = 2\pi n/L_z$, $n = 0\pm1, \ldots, \pm6$. Potential contours in $x-y$ with $k_y\rho_s = 0.392$ and a) $n = 0$, b) $n = 1$, c) $n = 2$, and d) $n = 4$.
22. 3D simulation results in the sheared case with $L_s/L_n = 14$, $v_d/c_s = 10$, and $k_z = 2\pi n/L_z$, $n = 0, \pm1, \ldots, \pm6$. Potential fluctuations versus time for $k_y\rho_s = 0.392$ and a) $n = 0$, b) $n = 2$, and c) $n = 4$. Magnitudes of potential fluctuations versus time for $k_y\rho_s = 0.392$ and d) $n = 0$, e) $n = 2$, and f) $n = 4$.
23. QLP geometry in $x - v_{||}$ for the shearless case. a) Diffusion paths, initial contours, and resonance region. b) Diffusion path deformation of the initial contour.
24. Comparison between simulation and QLP theory for the saturation amplitude of the potential fluctuations in the shearless case.
25. QLP geometry in $x - v_{||}$ for the sheared case with a) $v_d/c_s = 6$ and b) $v_d/c_s = 12$. The diffusion paths, initial contours, and the resonance regions are depicted.
26. Comparison between a) simulation and b) QLP theory for the saturated state contours in $x - v_{||}$, where $L_s/L_n = 14$, $v_d/c_s = 8$, and $k_y\rho_s = 0.392$.
27. Comparison between simulation and QLP theory for the saturation amplitude of the potential fluctuations in the sheared case.

28. Electron trajectories in $x - v_{||}$ for the sheared 3D case. The dots in d) are used for a regression analysis to compare simulation to QLP theory of the electron diffusion paths.

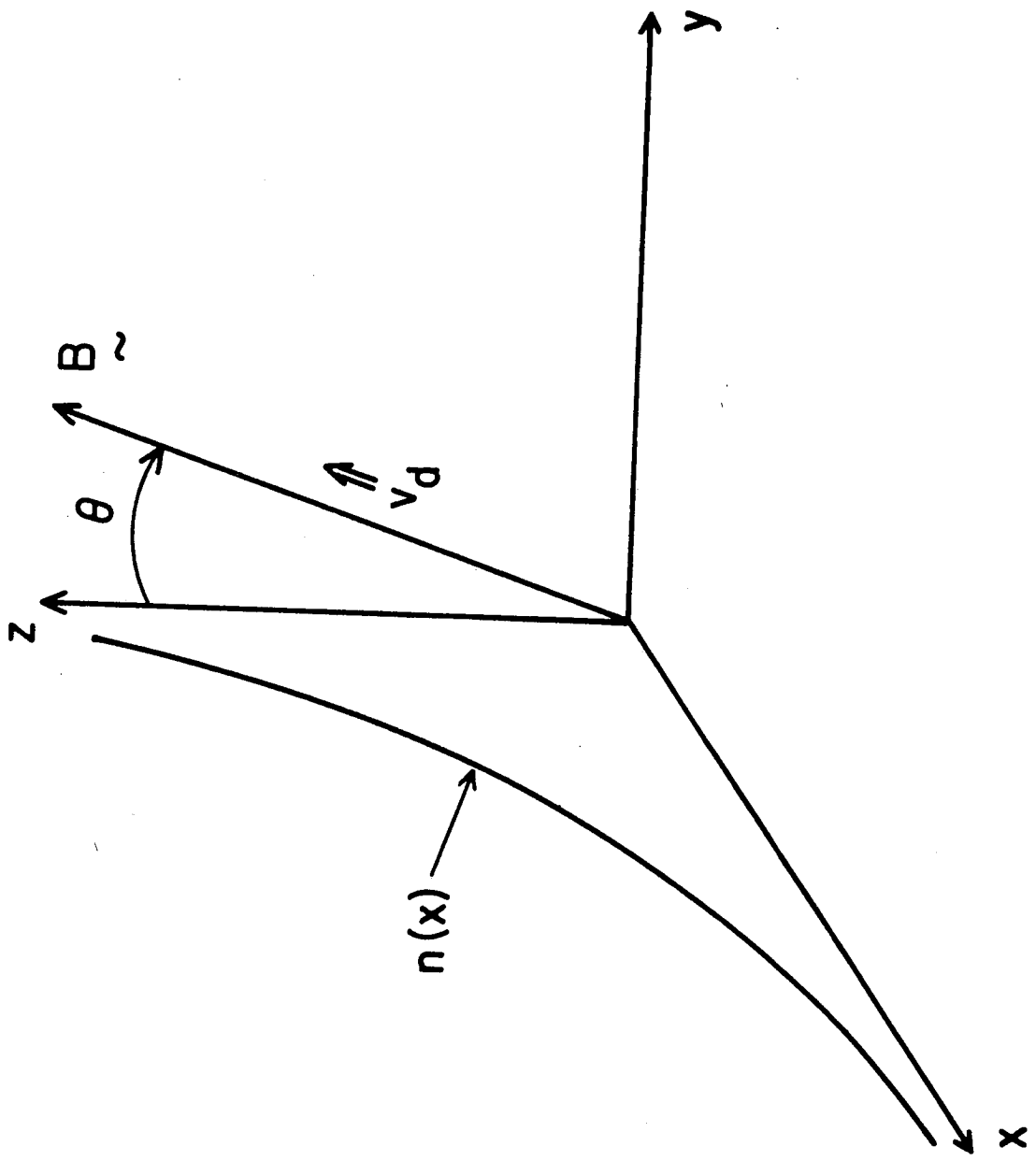

Fig. 1

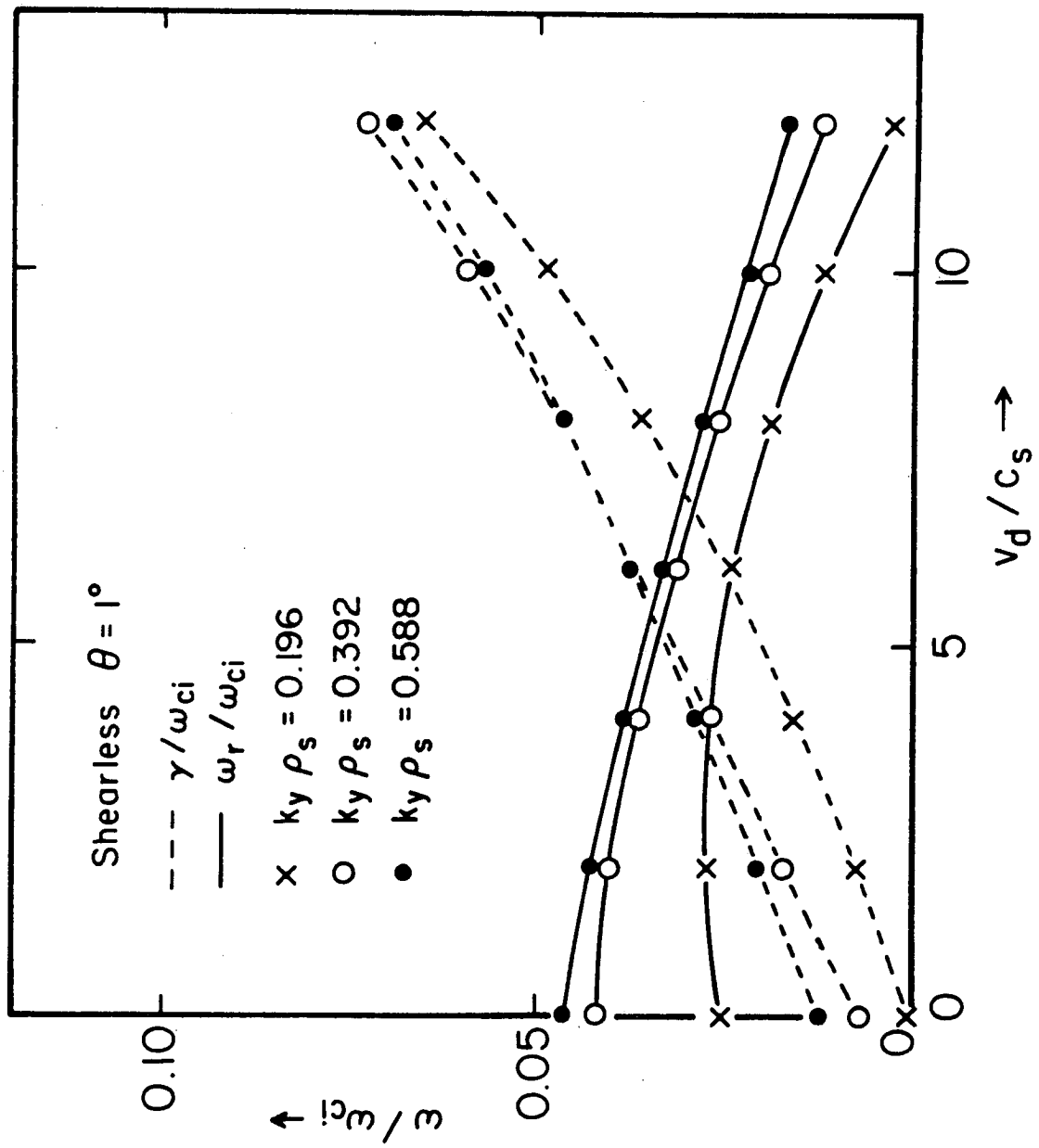
Shearless θ = 1°
--- γ/ω_ci
—— ω_r/ω_ci
× k_y ρ_s = 0.196
○ k_y ρ_s = 0.392
● k_y ρ_s = 0.588
γ/ω_ci →
0.10
0.05
0
5
10
v_d/c_s →

Fig. 2

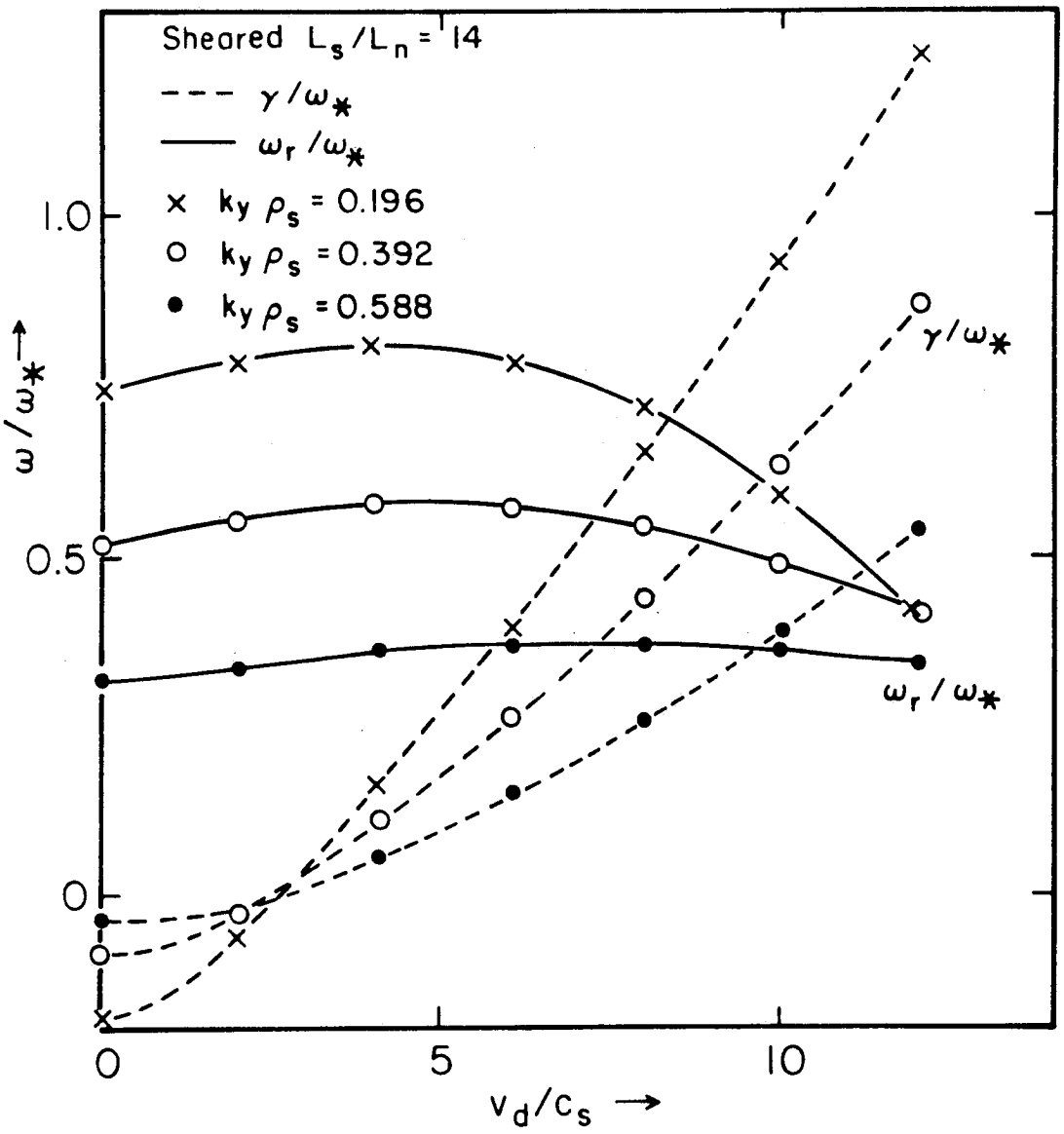
Sheared $L_s/L_n = 14$
γ/ω_*
ω_r/ω_*
$k_y \rho_s = 0.196$
$k_y \rho_s = 0.392$
$k_y \rho_s = 0.588$
ω/ω_*
1.0
0.5
0
0
5
10
v_d/c_s
γ/ω_*
ω_r/ω_*

Fig. 3

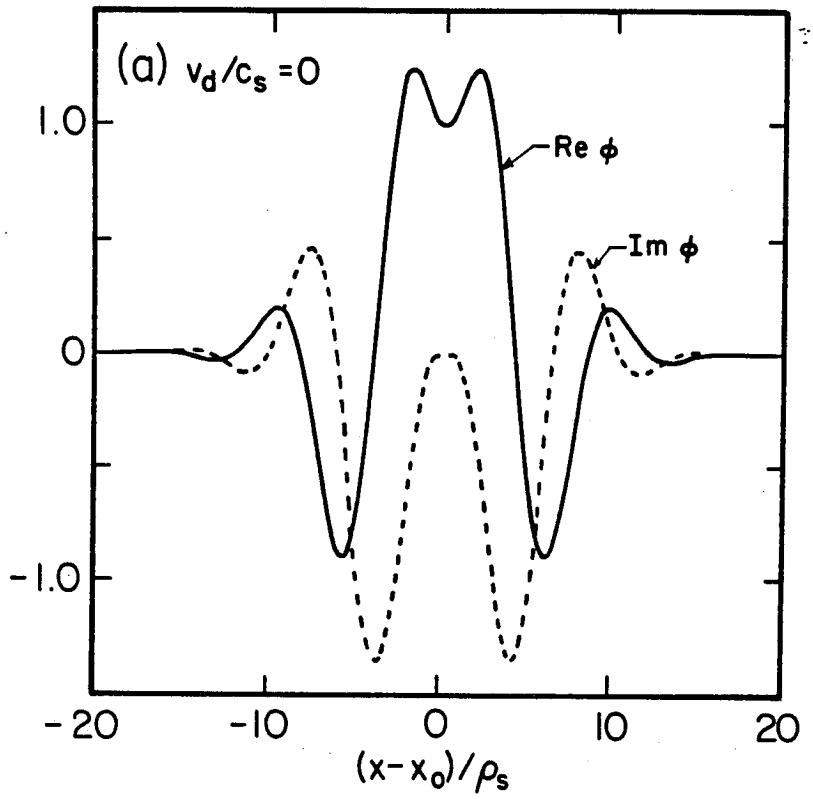
(a) $v_d/c_s = 0$
Re ϕ
Im ϕ
1.0
0
-1.0
-20
-10
0
10
20
$(x-x_0)/\rho_s$

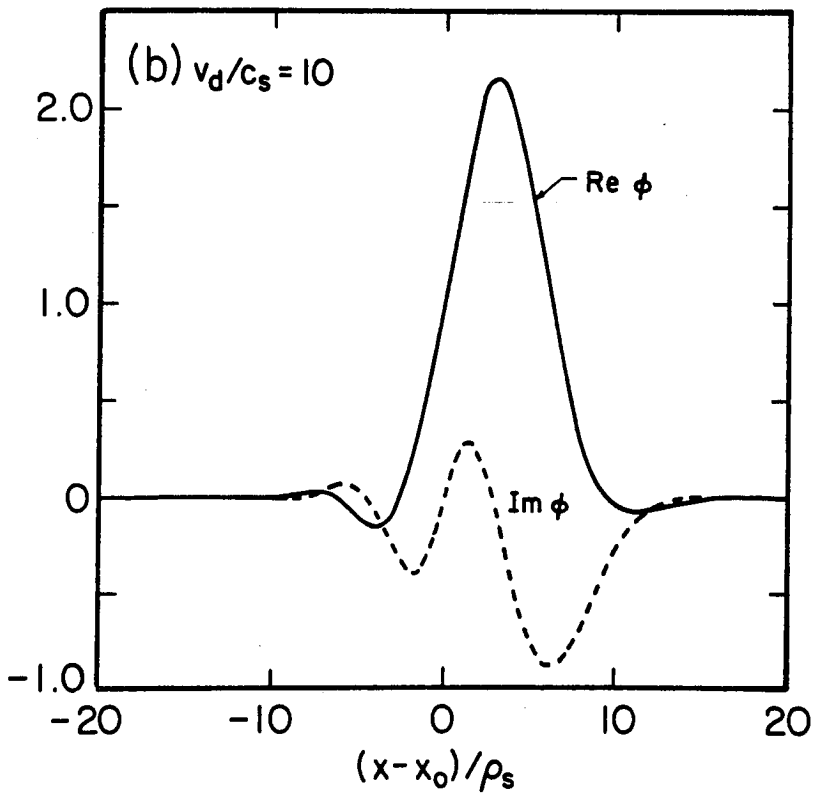
(b) $v_d/c_s = 10$
Re ϕ
Im ϕ
2.0
1.0
0
-1.0
-20
-10
0
10
20
$(x-x_0)/\rho_s$

Fig. 4

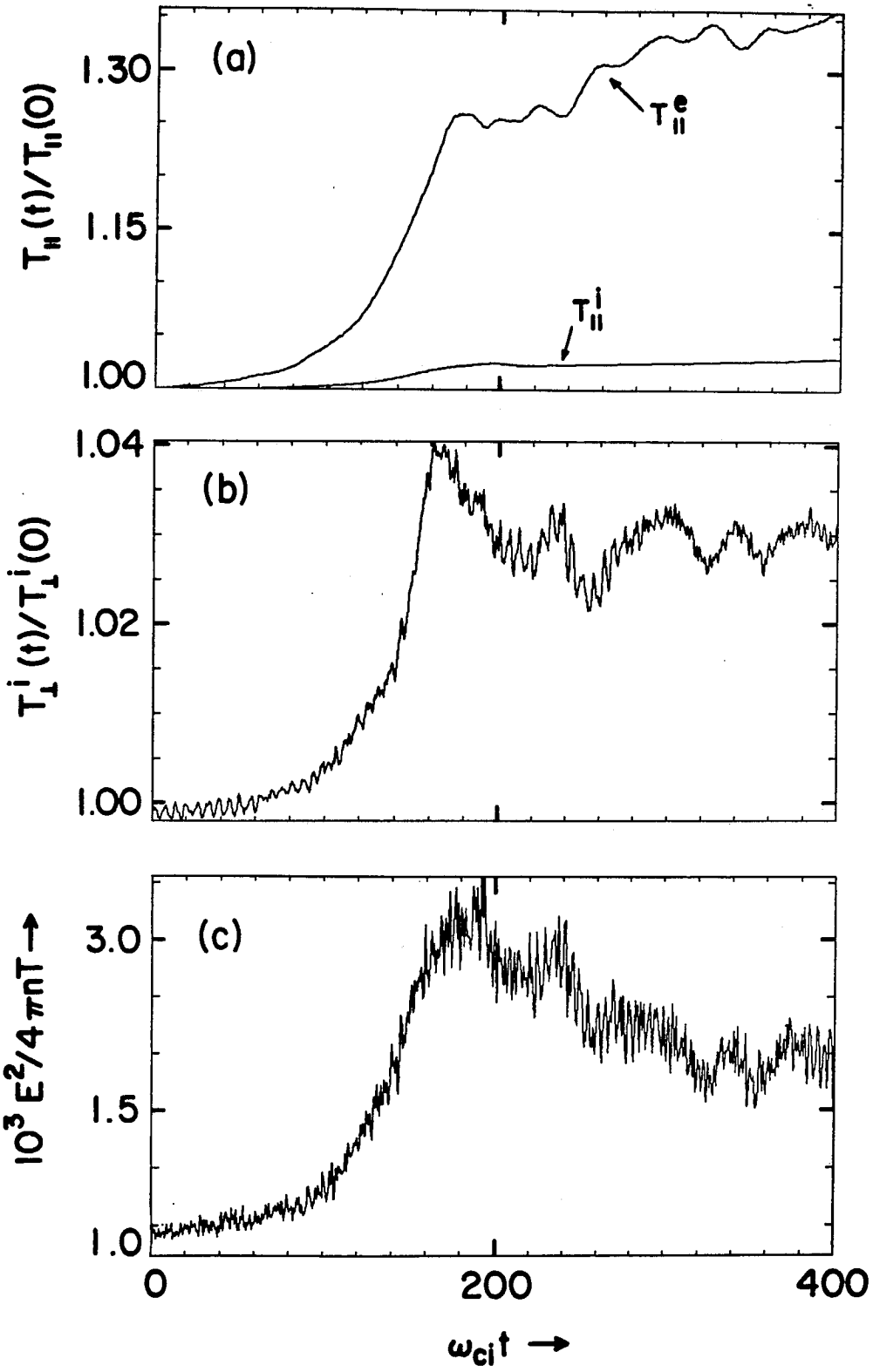
(a)
1.30
1.15
1.00
$T_{\parallel}(t)/T_{\parallel}(0)$
$T_{\parallel}^{e}$
$T_{\parallel}^{i}$
(b)
1.04
1.02
1.00
$T_{\perp}^{i}(t)/T_{\perp}^{i}(0)$
(c)
3.0
1.5
1.0
$10^3 E^2/4\pi nT \rightarrow$
0
200
400
$\omega_{ci} t \rightarrow$

Fig. 5

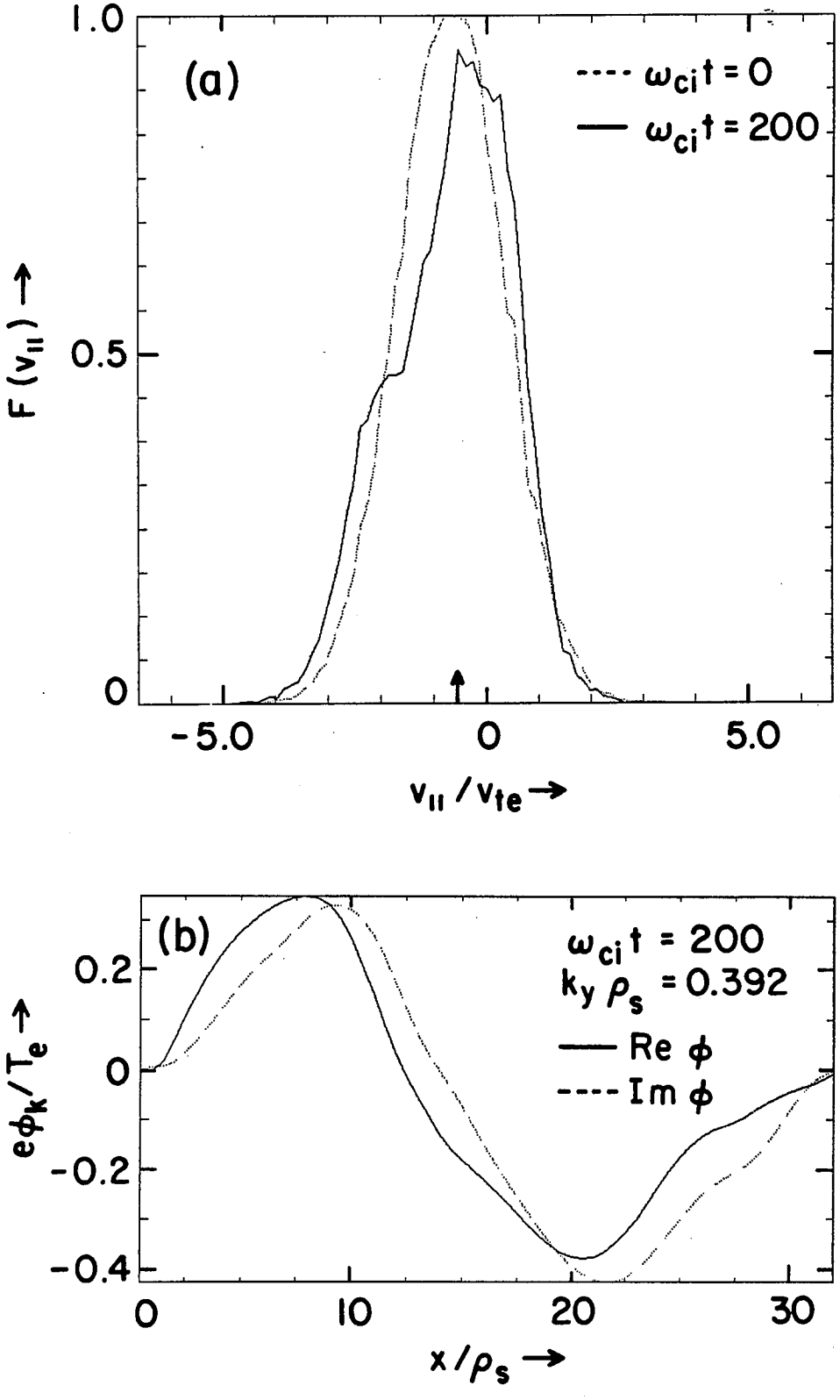
(a)
$\omega_{ci}t = 0$
$\omega_{ci}t = 200$
1.0
0.5
0
$F(v_{||})$ →
-5.0
0
5.0
$v_{||}/v_{te}$ →
(b)
$\omega_{ci}t = 200$
$k_y \rho_s = 0.392$
Re ϕ
Im ϕ
0.2
0
-0.2
-0.4
$e\phi_k/T_e$ →
0
10
20
30
x/ρ_s →

Fig. 6

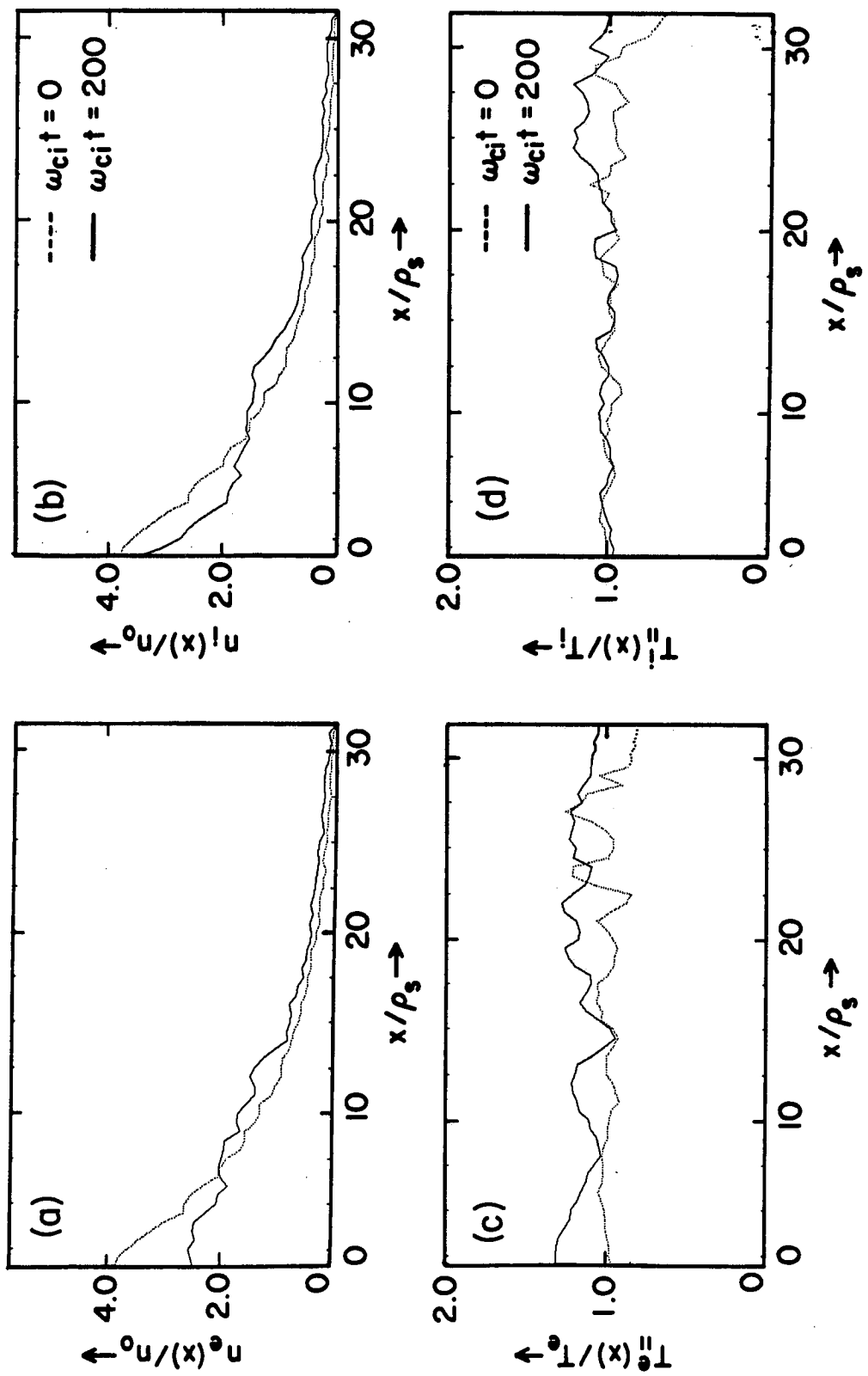
(a)
(b)
(c)
(d)
$\omega_{ci}t = 0$
$\omega_{ci}t = 200$
$n_e(x)/n_o$
$n_i(x)/n_o$
$T_{\parallel}^e(x)/T_e$
$T_{\parallel}^i(x)/T_i$
x/ρ_s
0
10
20
30
2.0
4.0
1.0

Fig. 7

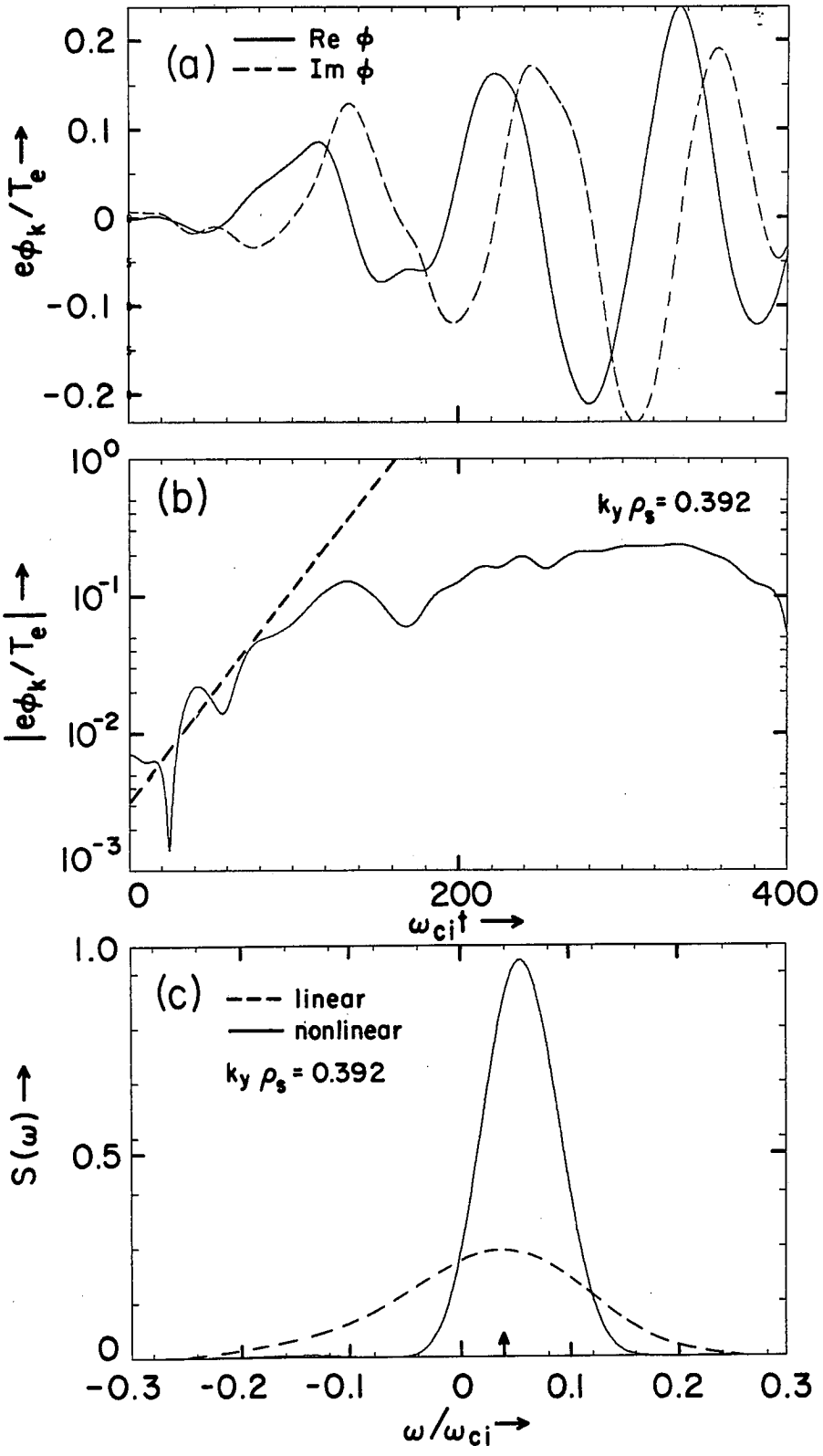
(a)
Re φ
Im φ
0.2
0.1
0
-0.1
-0.2
eφk/Te
(b)
ky ρs = 0.392
10^0
10^-1
10^-2
10^-3
|eφk/Te|
0
200
400
ωci t
(c)
linear
nonlinear
ky ρs = 0.392
1.0
0.5
0
S(ω)
-0.3
-0.2
-0.1
0
0.1
0.2
0.3
ω/ωci

Fig. 8

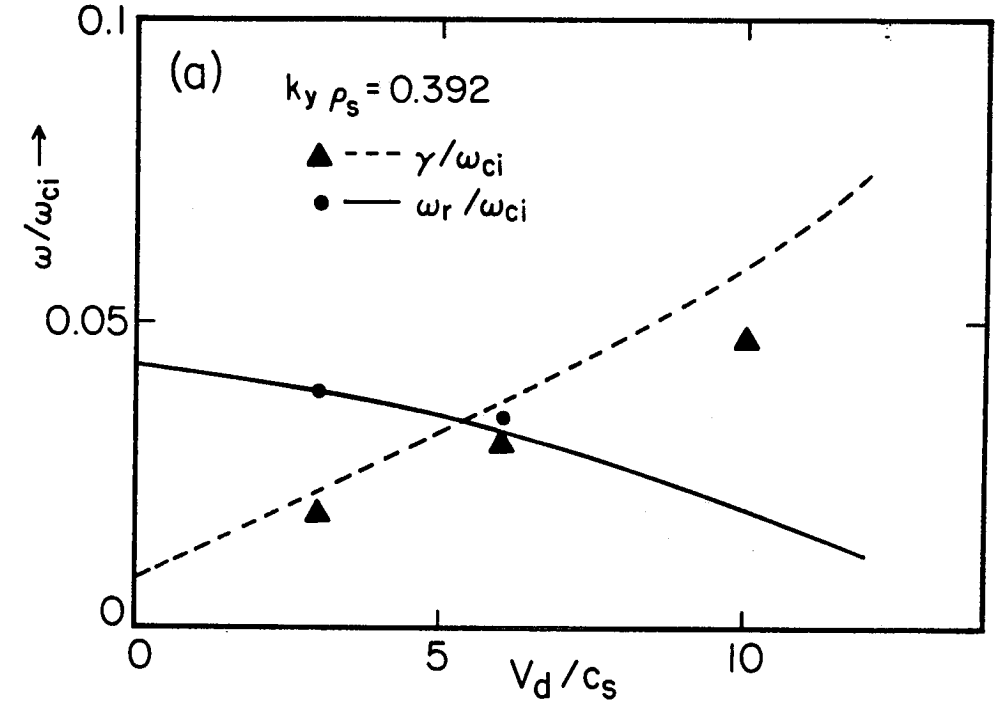
(a)
$k_y \rho_s = 0.392$
γ/ω_{ci}
ω_r/ω_{ci}
ω/ω_{ci}
0.1
0.05
0
0
5
10
V_d/c_s

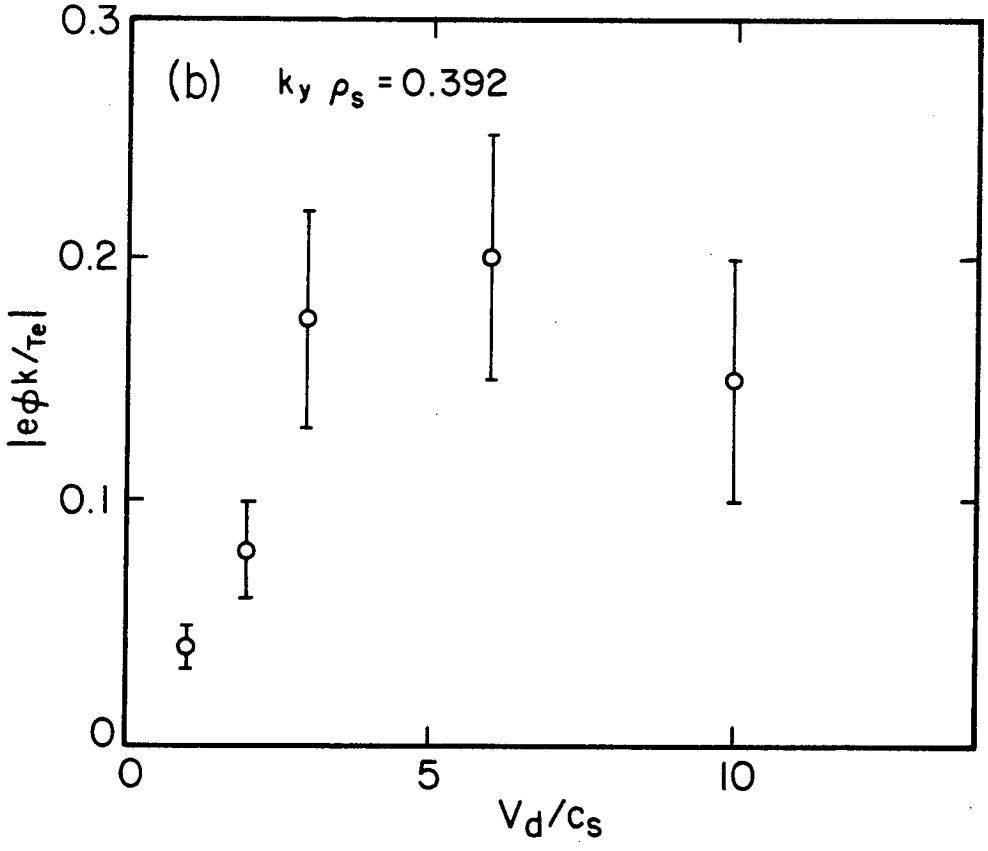
(b)
$k_y \rho_s = 0.392$
$|e\phi k/T_e|$
0.3
0.2
0.1
0
0
5
10
V_d/c_s

Fig. 9

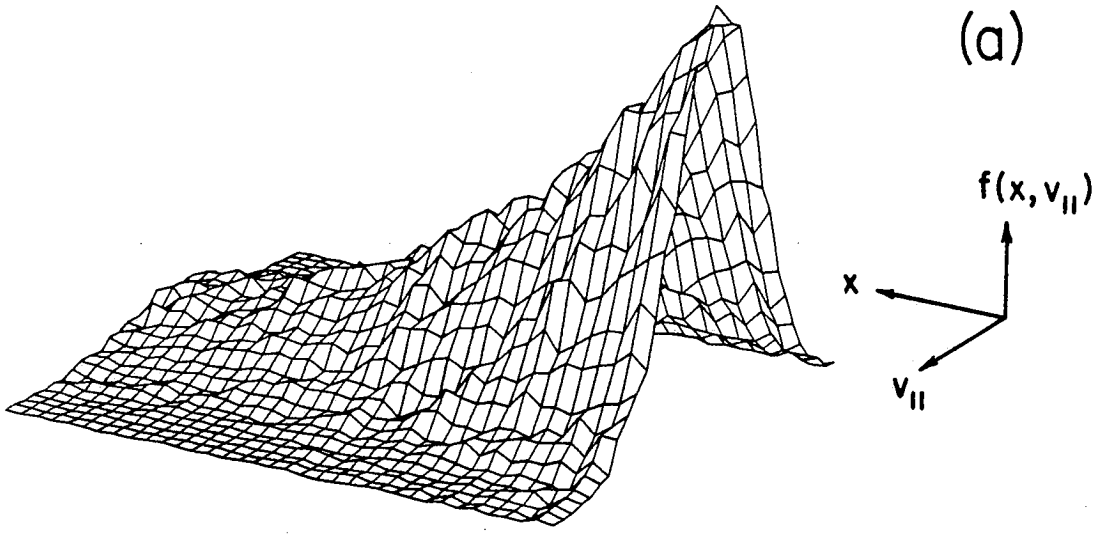

$\omega_{ci}t = 40$

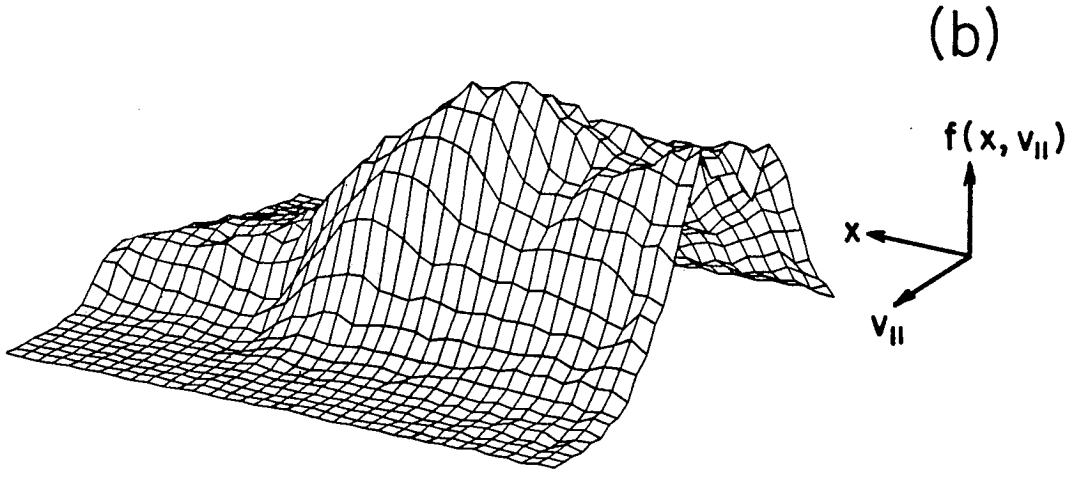

$\omega_{ci}t = 200$

Fig. 10

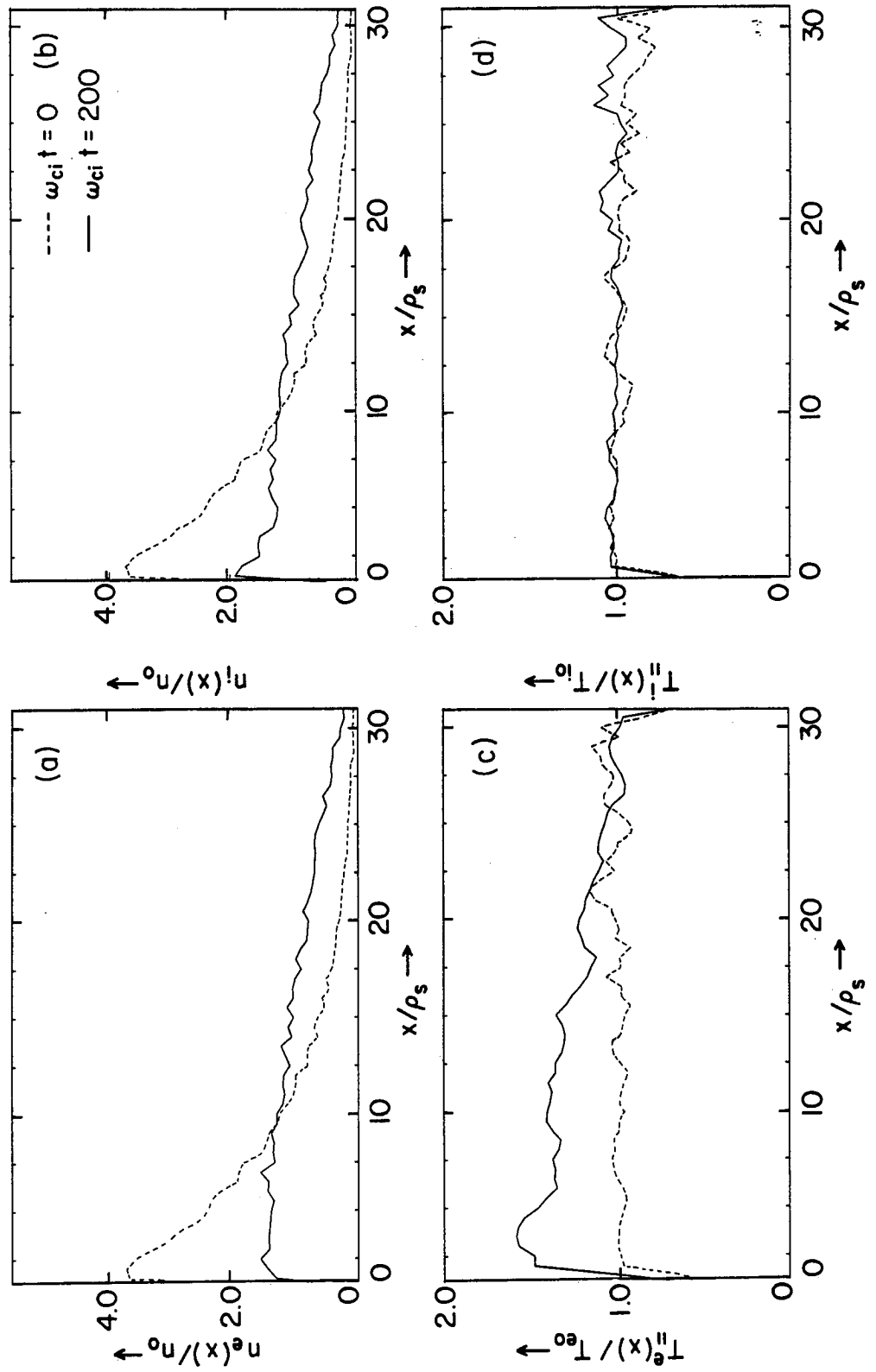
(a)
(b)
(c)
(d)
$\omega_{ci} t = 0$
$\omega_{ci} t = 200$
$n_e(x)/n_o$
$n_i(x)/n_o$
$T_{\parallel}^e(x)/T_{eo}$
$T_{\parallel}^i(x)/T_{io}$
x/ρ_s
0
10
20
30
0.0
2.0
4.0
1.0

Fig. 11

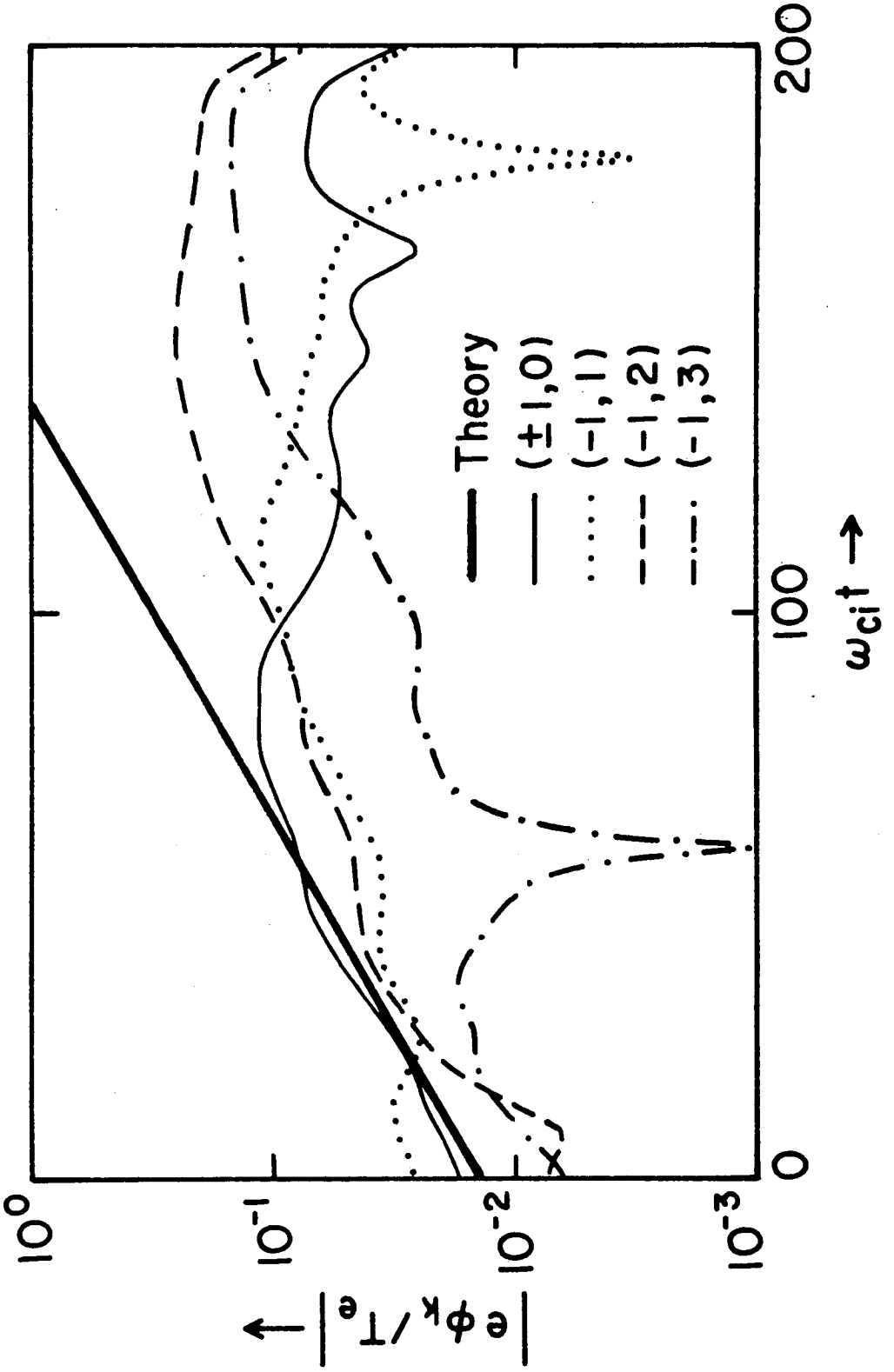
Theory
(±1,0)
(-1,1)
(-1,2)
(-1,3)
10^0
10^{-1}
10^{-2}
10^{-3}
$|e\phi_k/T_e| \rightarrow$
0
100
200
$\omega_{ci}t \rightarrow$

Fig. 12

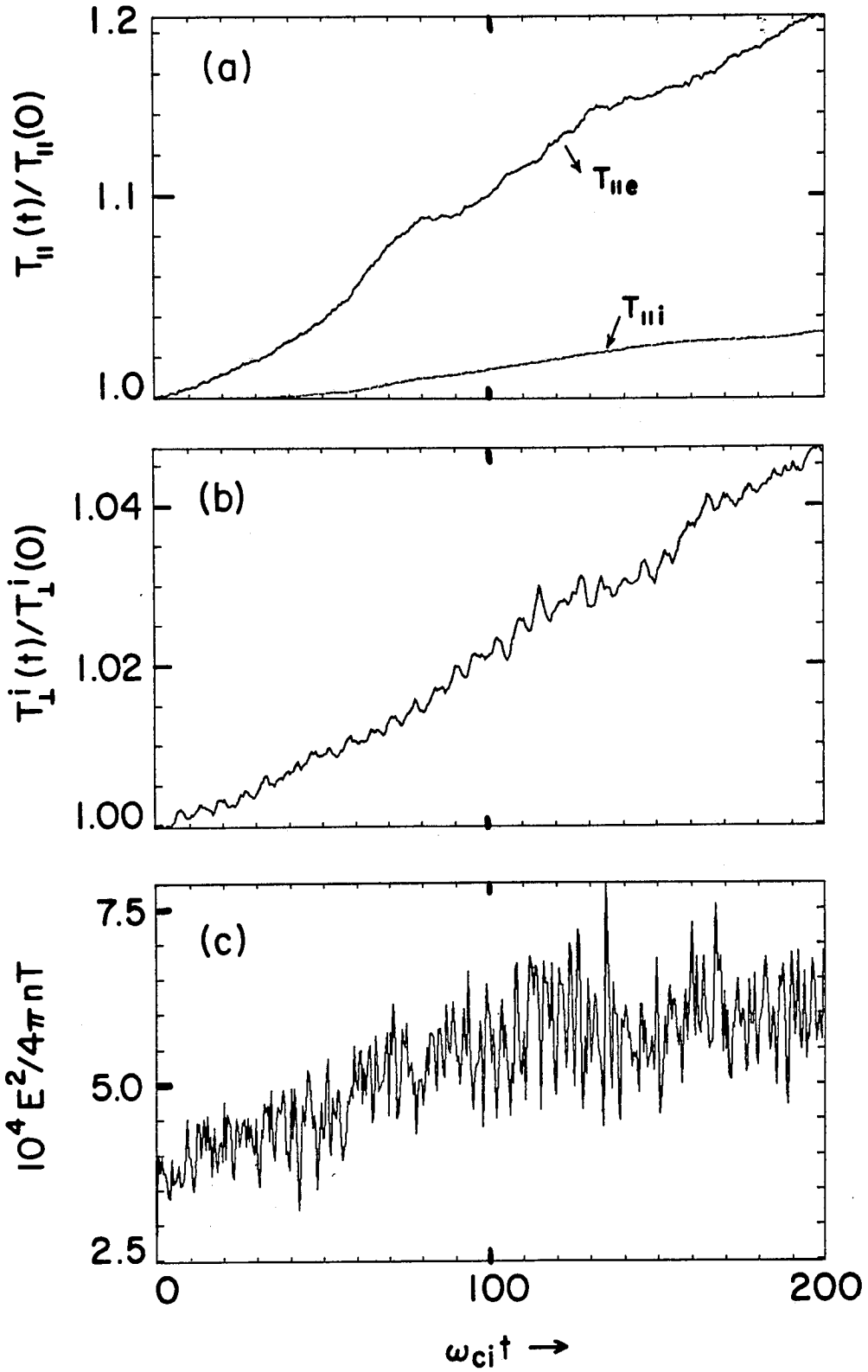
(a)
$T_{\parallel}(t)/T_{\parallel}(0)$
1.2
1.1
1.0
$T_{\parallel e}$
$T_{\parallel i}$
(b)
$T_{\perp}^{i}(t)/T_{\perp}^{i}(0)$
1.04
1.02
1.00
(c)
$10^4 E^2/4\pi nT$
7.5
5.0
2.5
0
100
200
$\omega_{ci} t \rightarrow$

Fig. 13

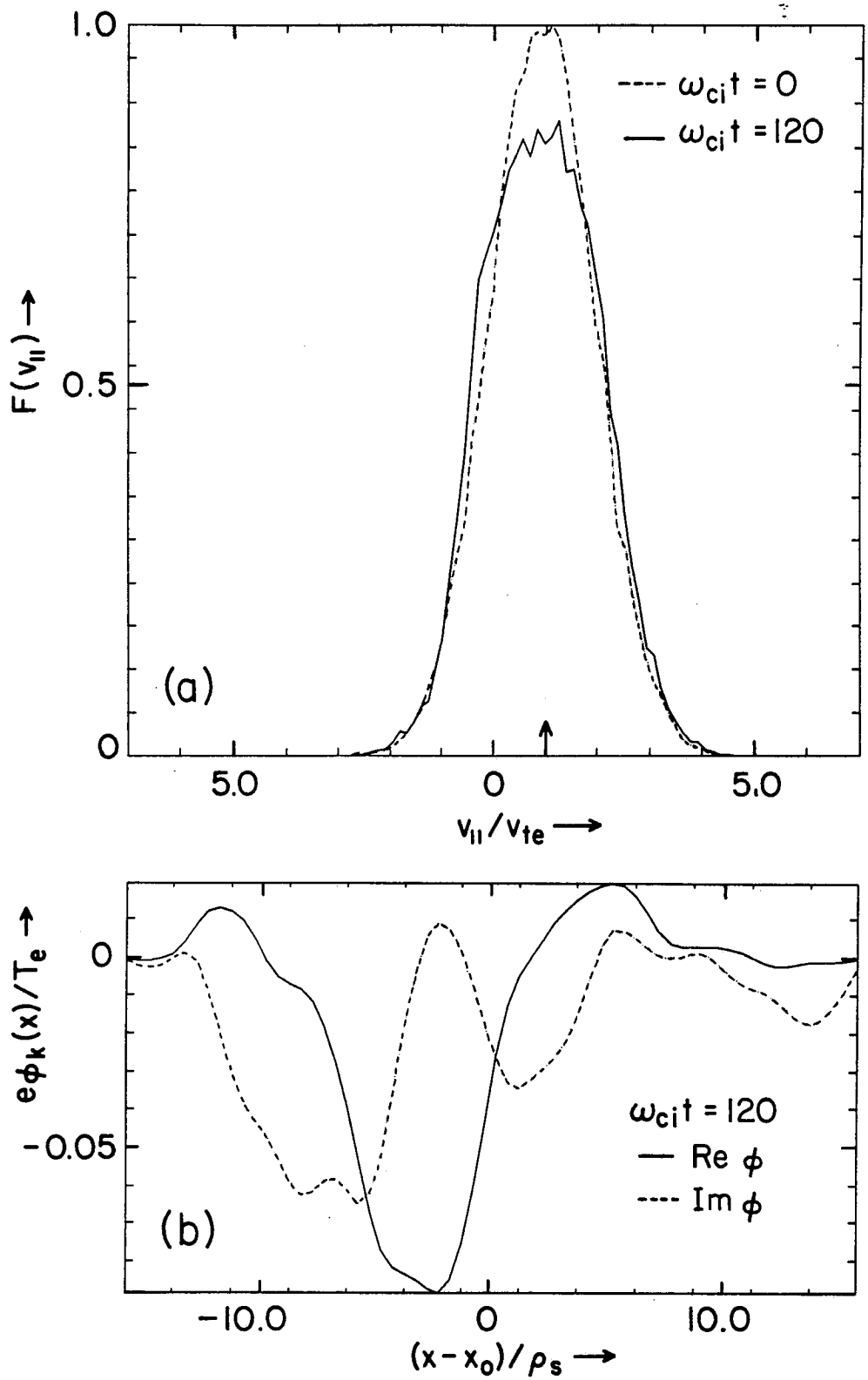
1.0
0.5
0
$F(v_{||})$ →
---- $\omega_{ci}t = 0$
— $\omega_{ci}t = 120$
(a)
5.0
0
5.0
$v_{||}/v_{te}$ →
$e\phi_k(x)/T_e$ →
0
-0.05
$\omega_{ci}t = 120$
— Re ϕ
---- Im ϕ
(b)
-10.0
0
10.0
$(x-x_0)/\rho_s$ →

Fig. 14

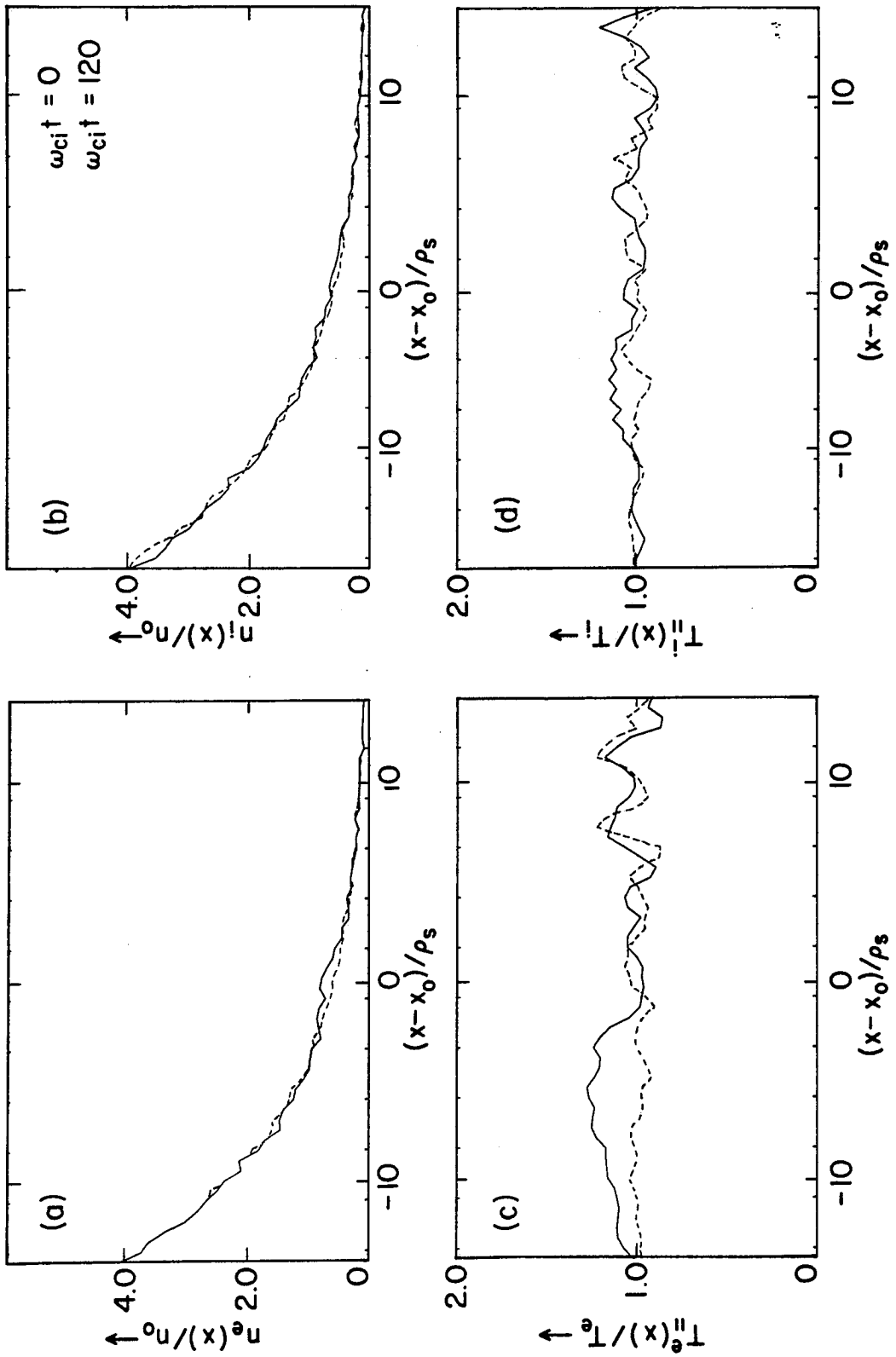
(a)
(b)
(c)
(d)
$\omega_{ci}t = 0$
$\omega_{ci}t = 120$
$n_e(x)/n_o$
$n_i(x)/n_o$
$T_{\parallel}^e(x)/T_e$
$T_{\parallel}^i(x)/T_i$
$(x-x_o)/\rho_s$
0
2.0
4.0
1.0
-10
10

Fig. 15

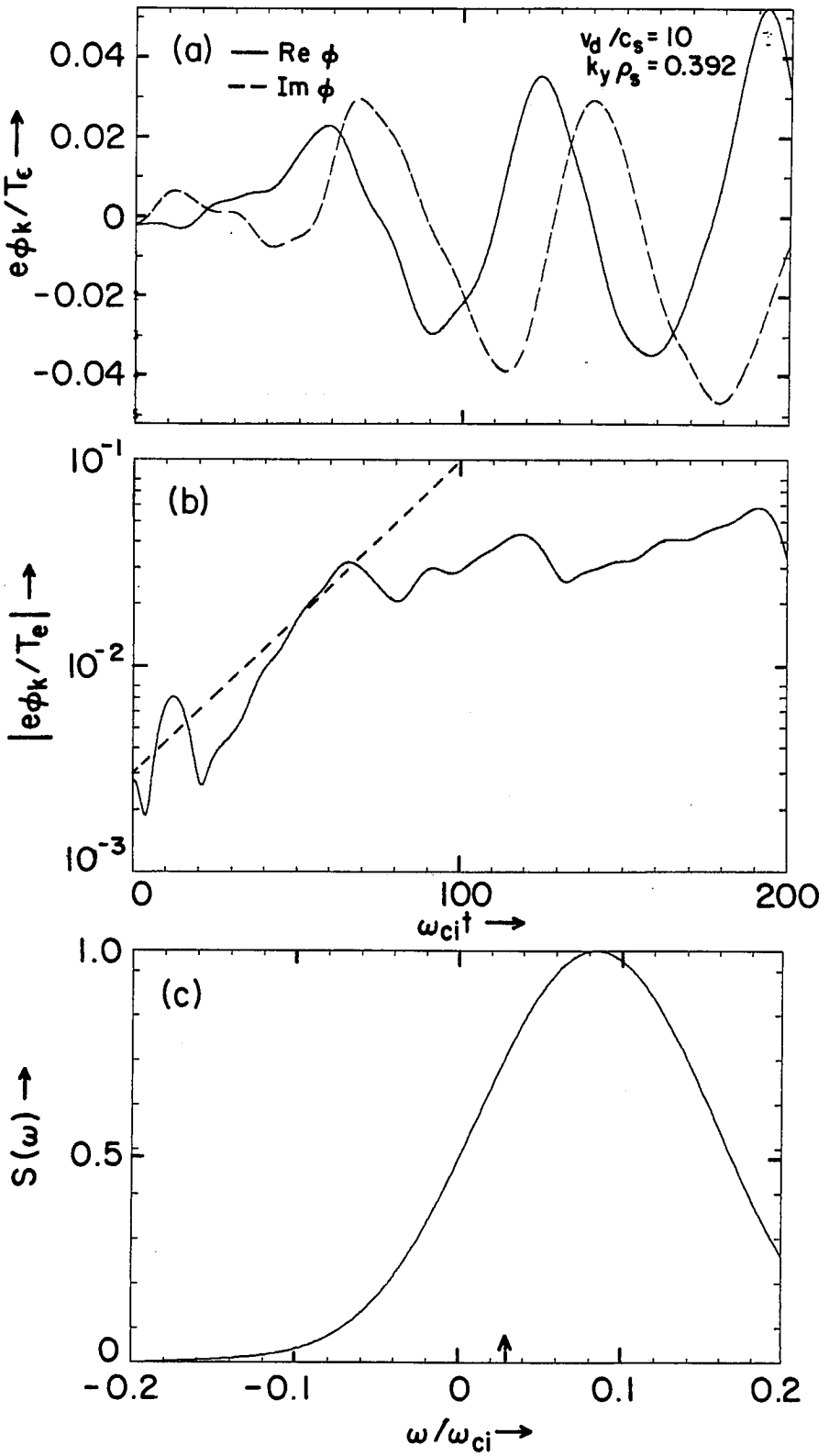
(a)
Re φ
Im φ
$v_d/c_s = 10$
$k_y\rho_s = 0.392$
0.04
0.02
0
-0.02
-0.04
$e\phi_k/T_e$
(b)
10^{-1}
10^{-2}
10^{-3}
$|e\phi_k/T_e|$
0
100
200
$\omega_{ci}t$
(c)
1.0
0.5
0
S(ω)
-0.2
-0.1
0
0.1
0.2
ω/ω_{ci}

Fig. 16

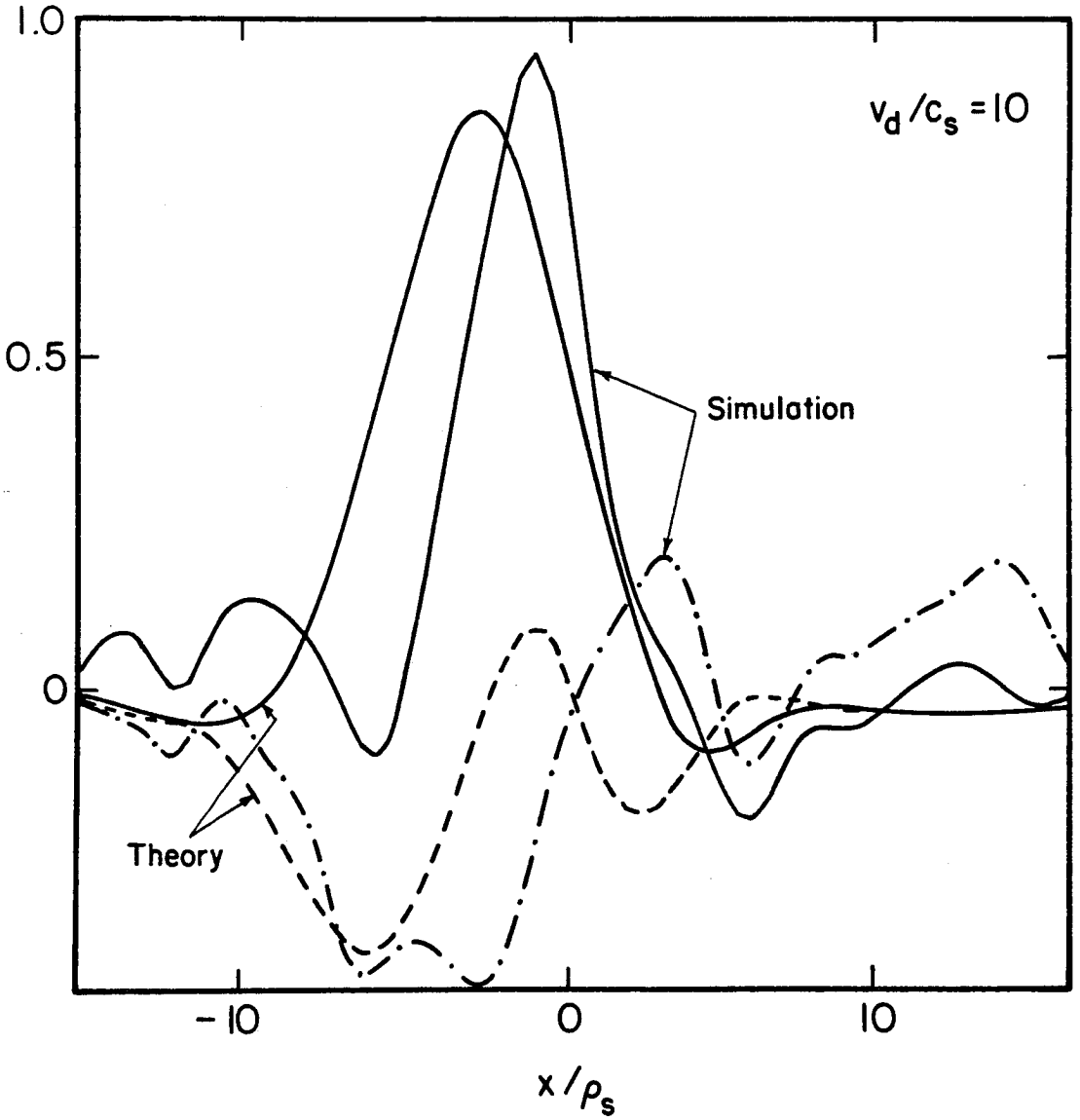

Fig. 17

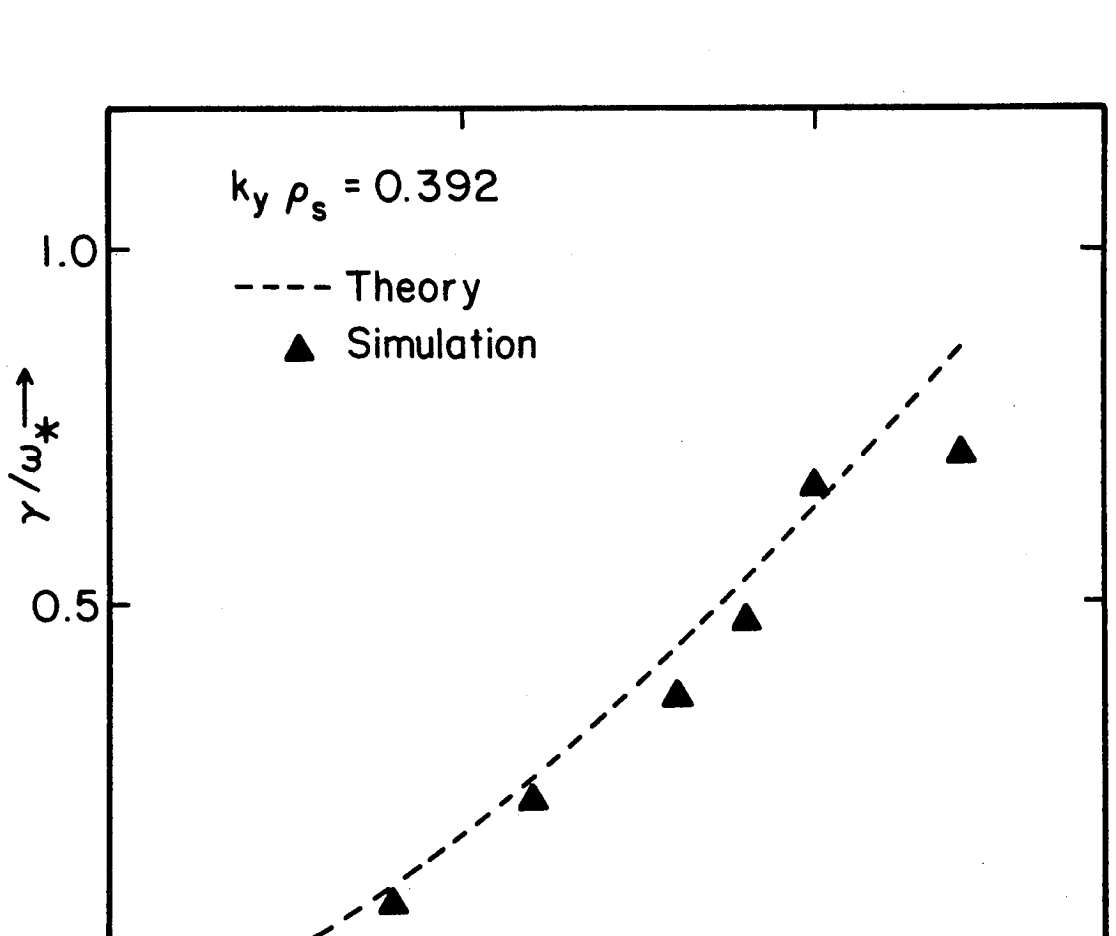

Fig. 18

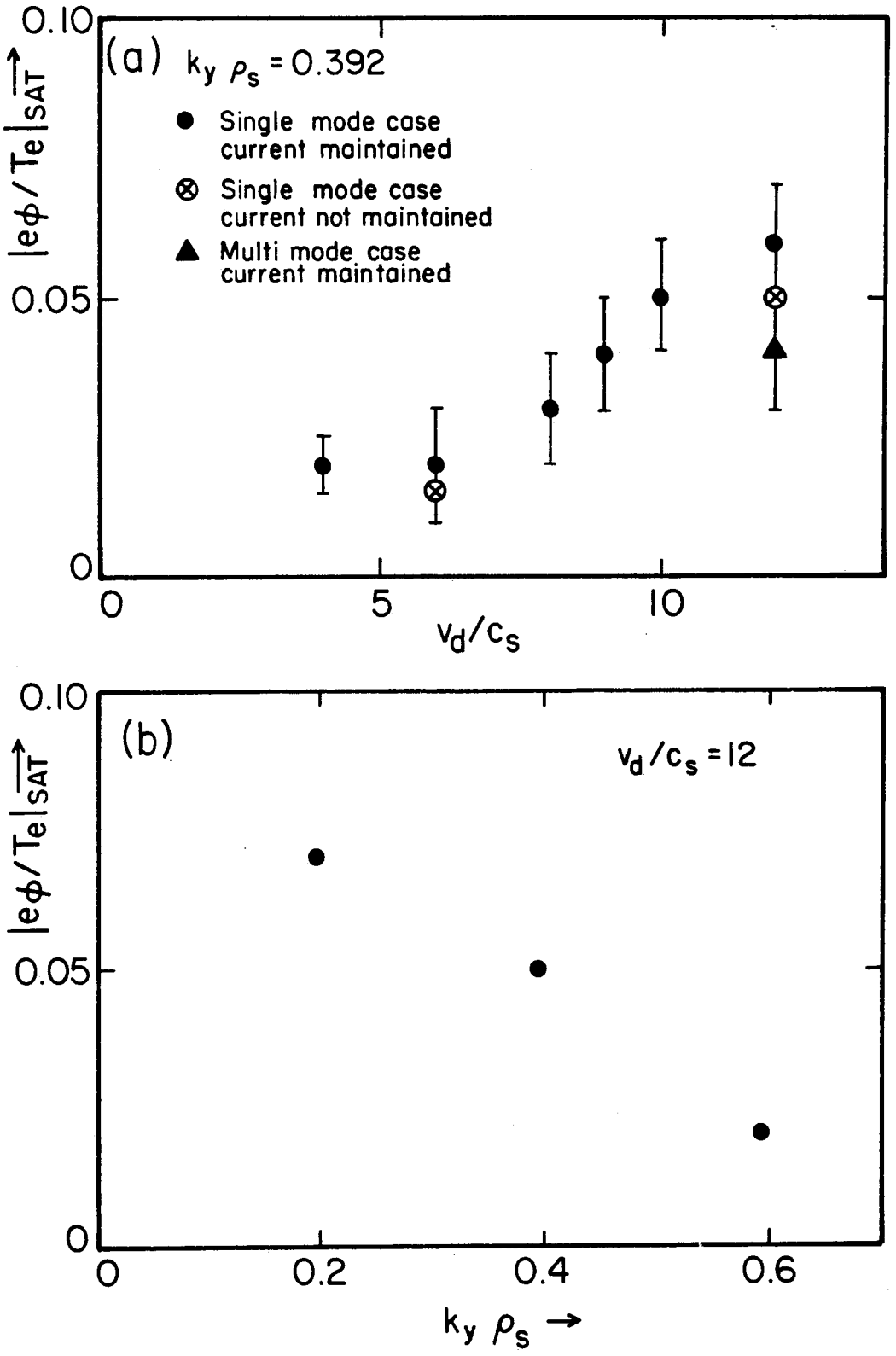
(a) $k_y \rho_s = 0.392$
Single mode case current maintained
Single mode case current not maintained
Multi mode case current maintained
$|e\phi/T_e|_{SAT}$
0.10
0.05
0
0
5
10
v_d/c_s
(b)
$v_d/c_s = 12$
$|e\phi/T_e|_{SAT}$
0.10
0.05
0
0
0.2
0.4
0.6
$k_y \rho_s \rightarrow$

Fig. 19

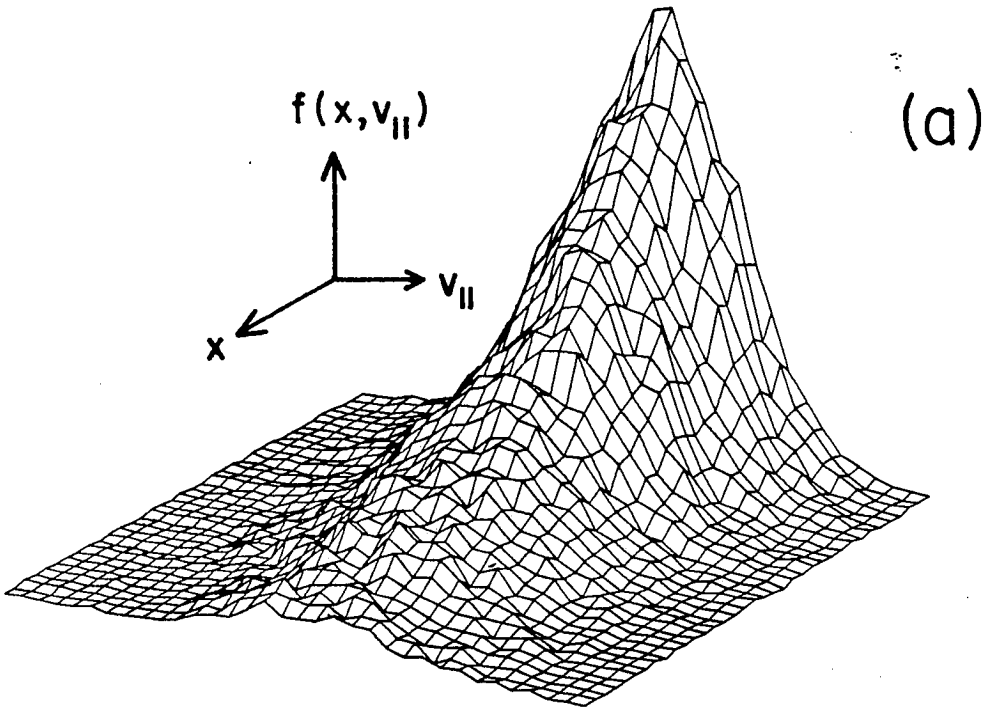

$\omega_{ci} t = 40$

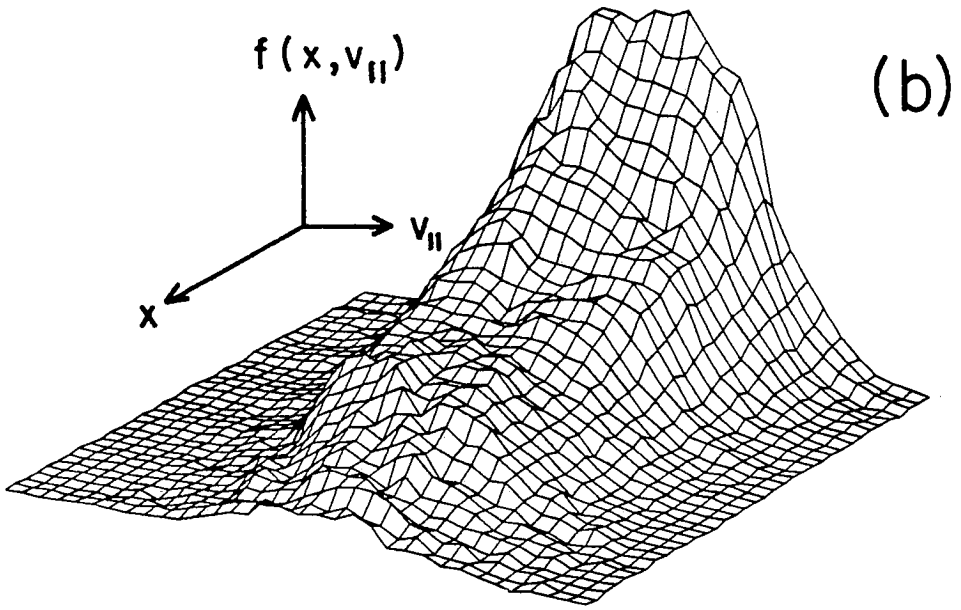

$\omega_{ci} t = 200$

Fig. 20

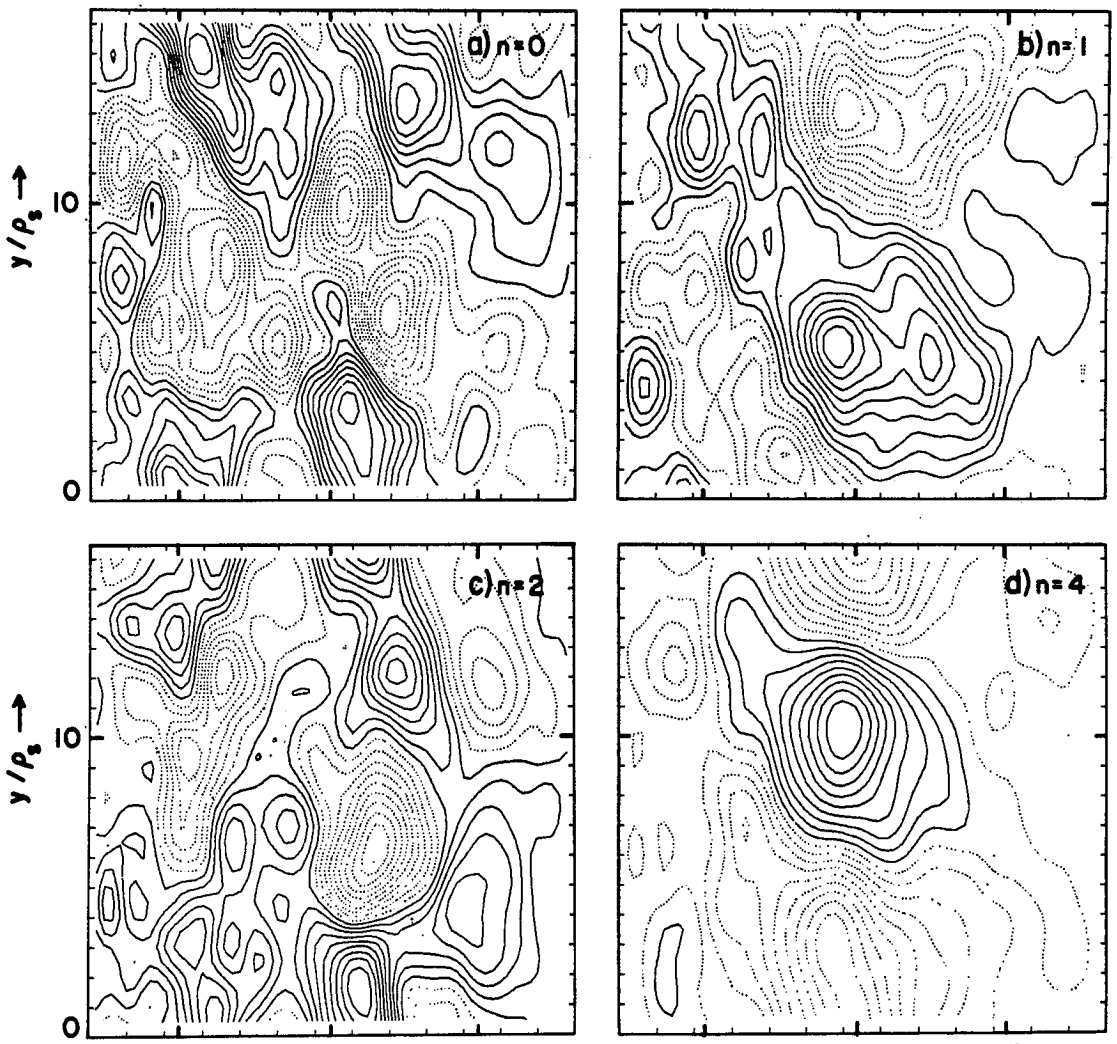

Fig. 21

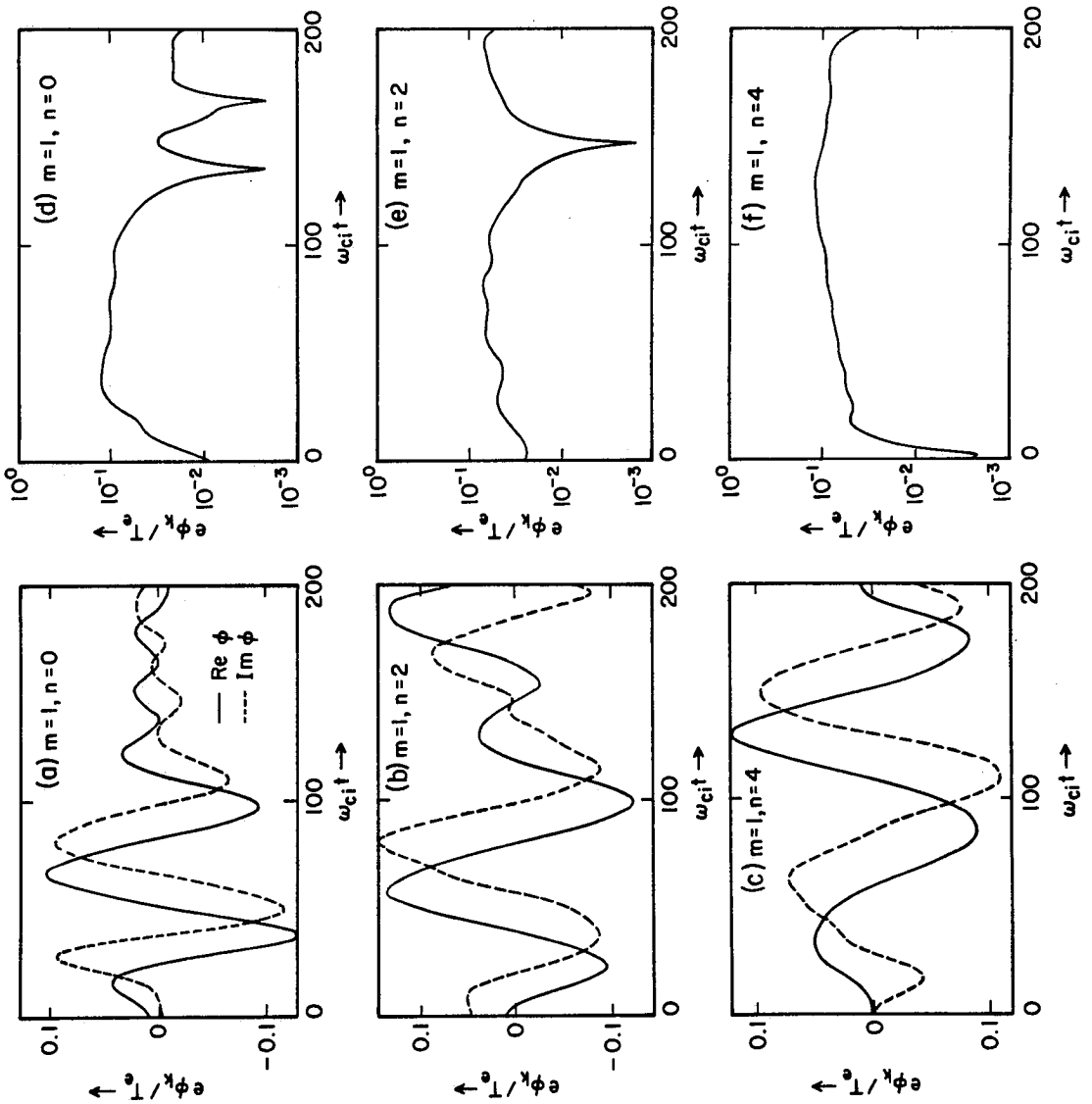

Fig. 22

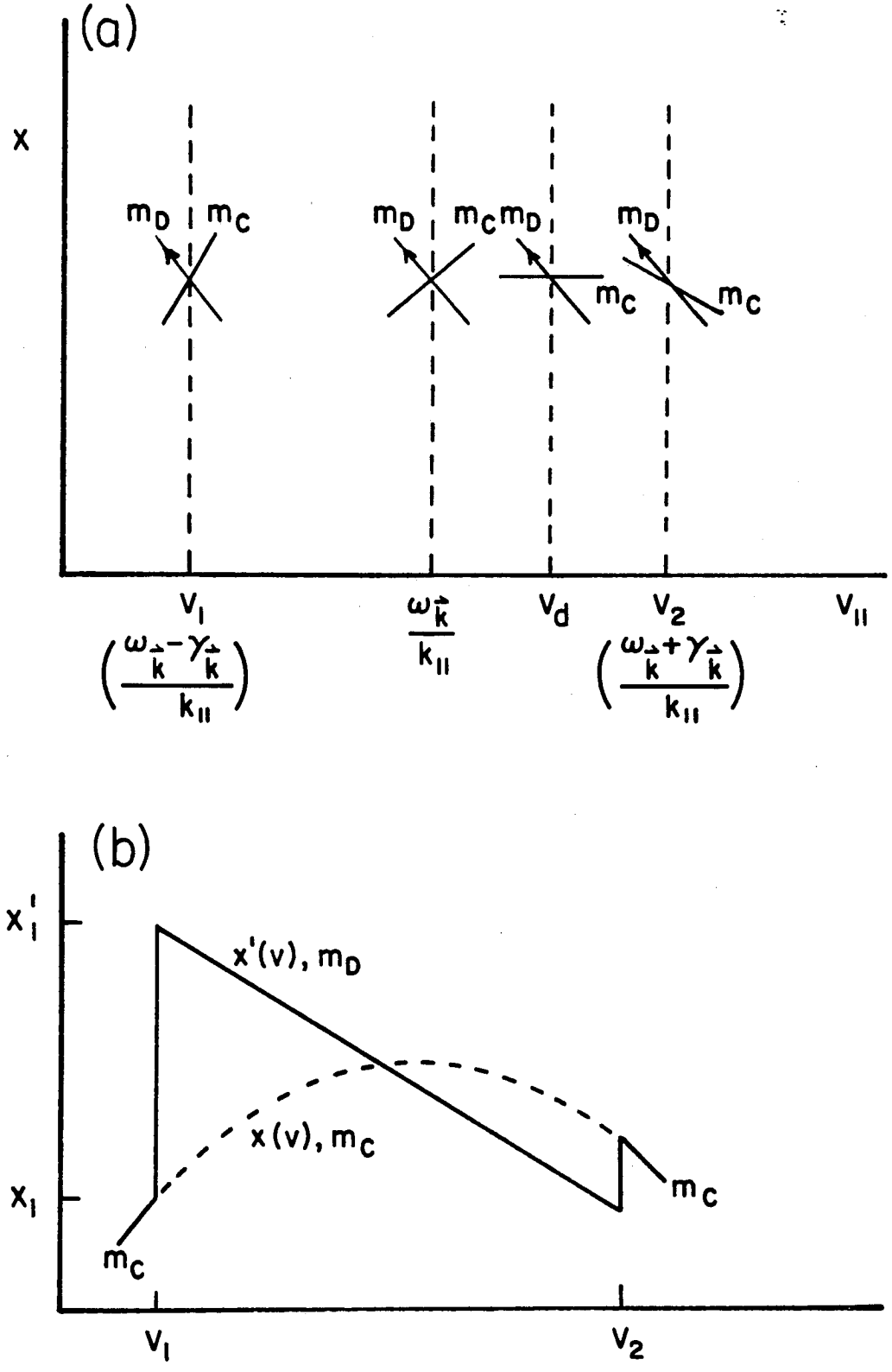
(a)
x
m_D
m_C
m_D
m_C
m_D
m_C
m_D
m_C
V_1
$\left(\frac{\omega_{\vec{k}}-\gamma_{\vec{k}}}{k_{\parallel}}\right)$
$\frac{\omega_{\vec{k}}}{k_{\parallel}}$
V_d
V_2
$\left(\frac{\omega_{\vec{k}}+\gamma_{\vec{k}}}{k_{\parallel}}\right)$
$V_{\parallel}$
(b)
x_1'
x_1
$x'(v), m_D$
$x(v), m_C$
m_C
m_C
V_1
V_2

Fig. 23

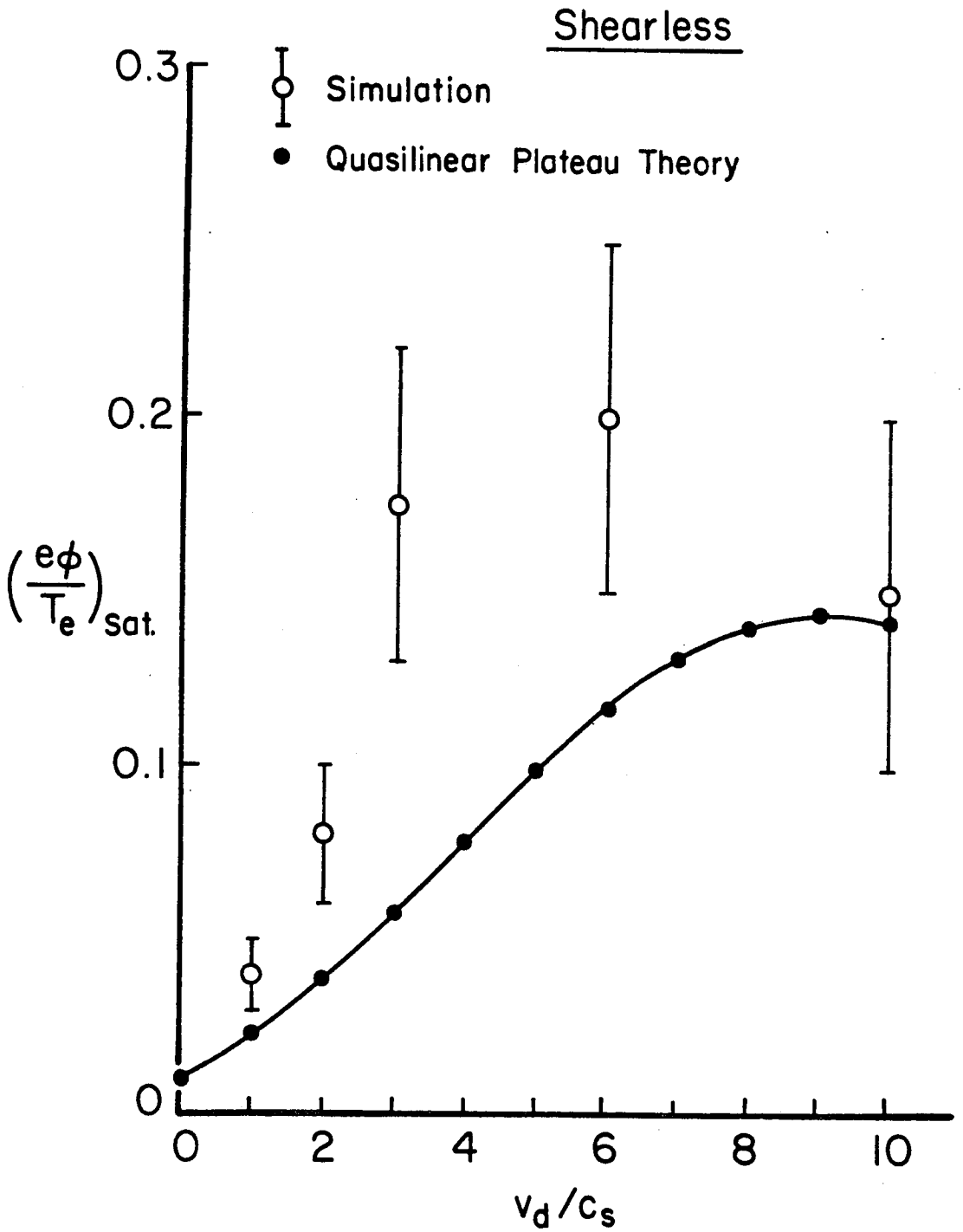
Shearless
Simulation
Quasilinear Plateau Theory
0.3
0.2
0.1
0
$\left(\frac{e\phi}{T_e}\right)_{sat.}$
0
2
4
6
8
10
v_d/c_s

Fig. 24

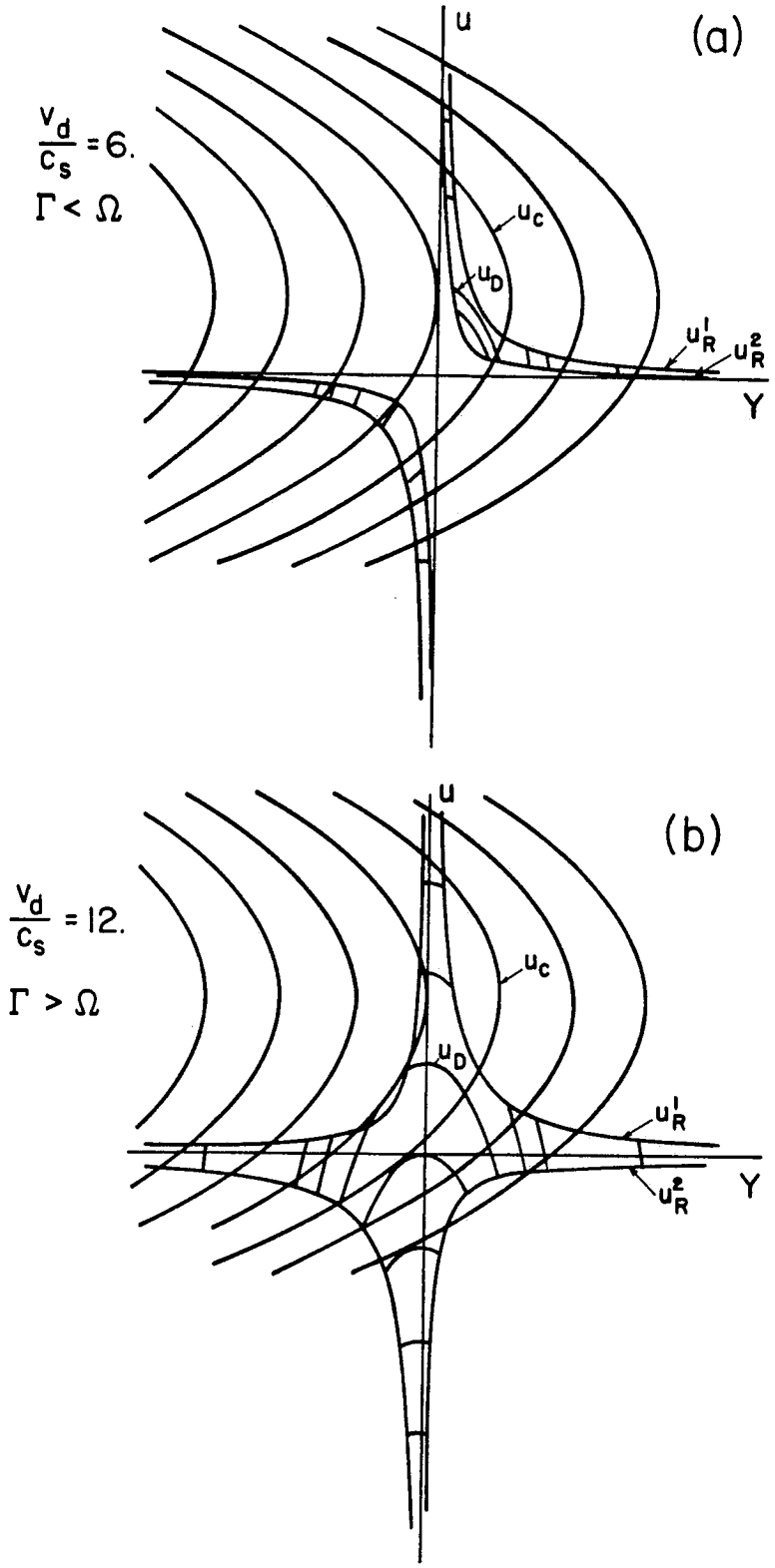
u
(a)
$\frac{v_d}{c_s} = 6.$
$\Gamma < \Omega$
u_c
u_D
u_R^1
u_R^2
Y
u
(b)
$\frac{v_d}{c_s} = 12.$
$\Gamma > \Omega$
u_c
u_D
u_R^1
u_R^2
Y

Fig. 25

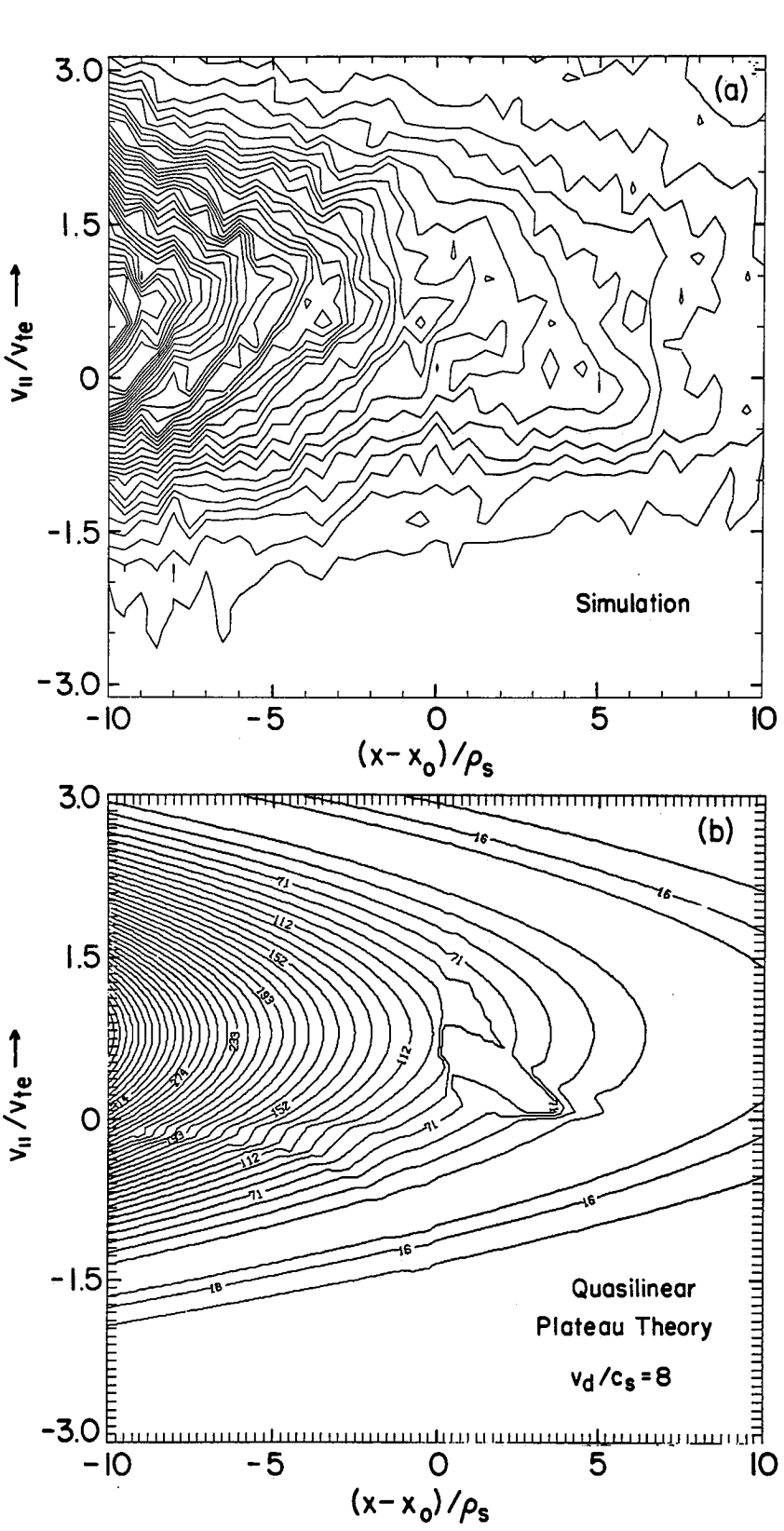
(a)
Simulation
(b)
Quasilinear
Plateau Theory
$v_d/c_s = 8$
$v_{\parallel}/v_{te}$
$(x-x_0)/\rho_s$
3.0
1.5
0
-1.5
-3.0
-10
-5
0
5
10
16
71
112
152
193
233
274
315

Fig. 26

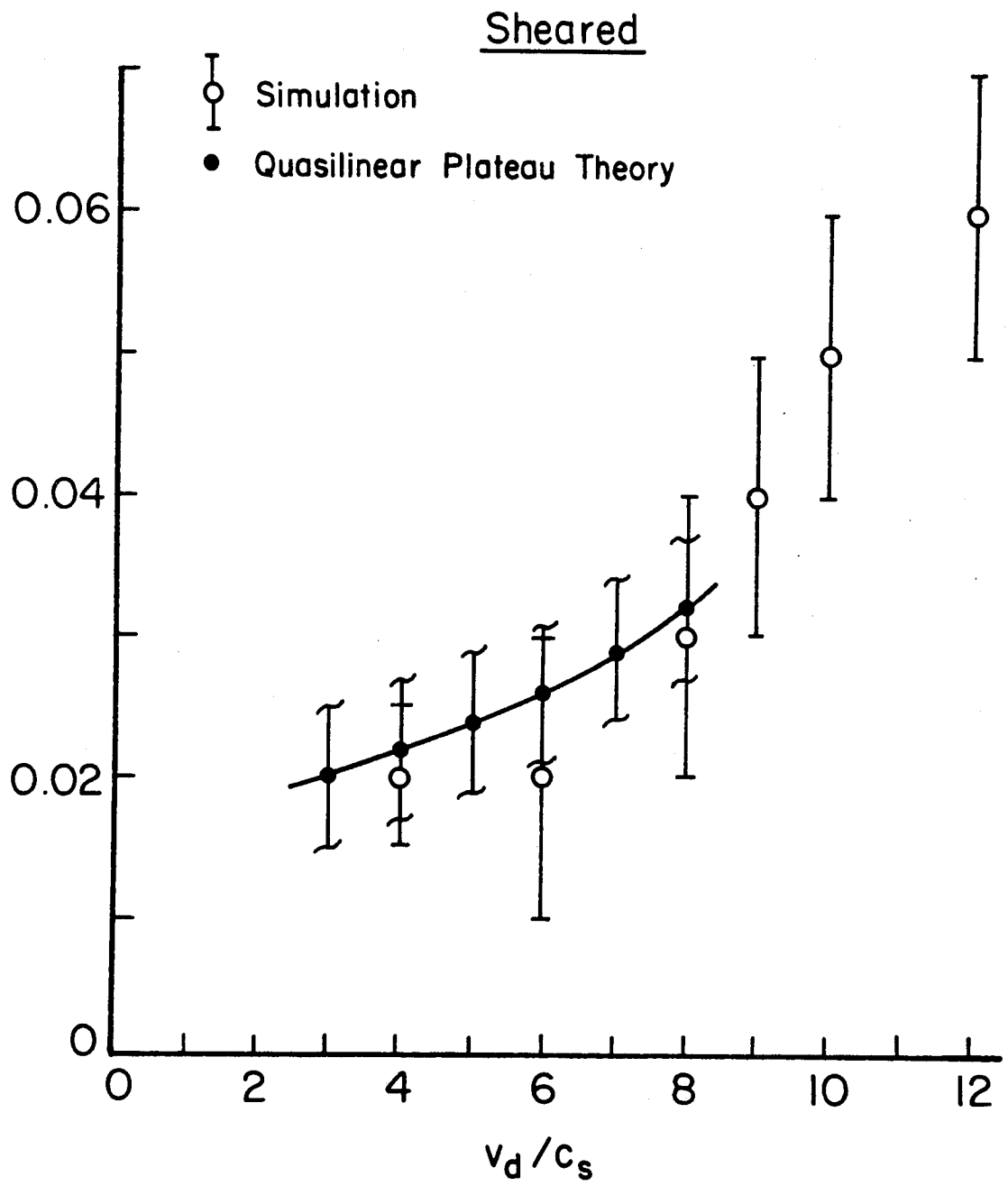
Sheared
Simulation
Quasilinear Plateau Theory
0.06
0.04
0.02
0
0
2
4
6
8
10
12
v_d/c_s

Fig. 27

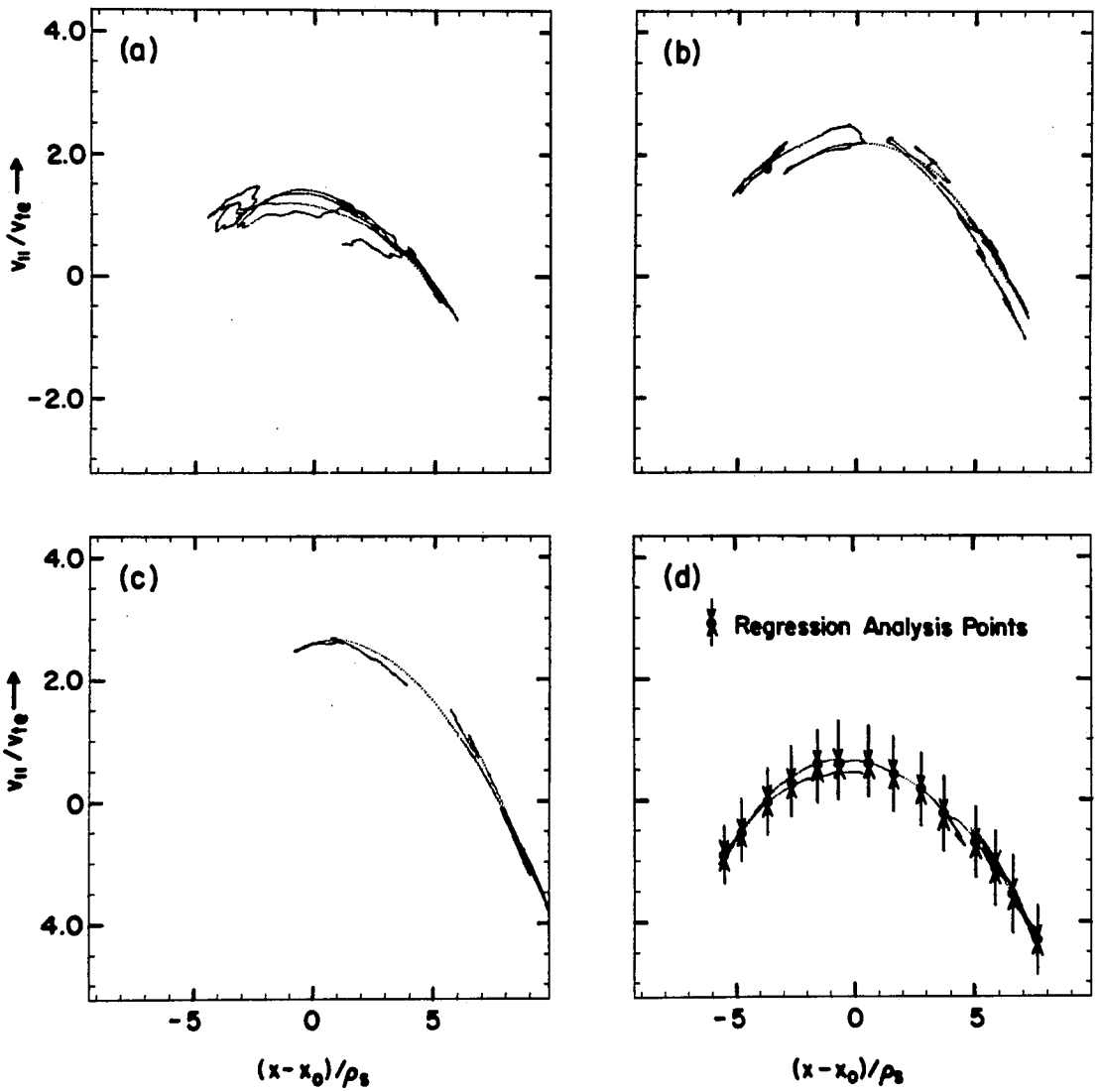
(a)
(b)
(c)
(d)
4.0
2.0
0
-2.0
4.0
$v_{\parallel}/v_{te}$
-5
0
5
$(x-x_0)/\rho_s$
Regression Analysis Points

Fig. 28